PCCP

PAPER

View Article Online
View Journal | View Issue

Cite this: *Phys. Chem. Chem. Phys.*, 2025, **27**, 23468

Tunable reducibility of alkaline earth metal clusters for carbon dioxide and nitrogen molecule activation: a QM-QSPR study

Natalia Wiszowska, [a] Natalia Rogoża [a] and Celina Sikorska *[ab]

A hybrid approach combining *ab initio* computational techniques of quantum chemistry with a machine learning strategy was used to design and investigate BAe_3 (Ae = Be, Mg, Ca, Sr, and Ba) molecular clusters with strong reducing abilities. In these systems, the type of electropositive alkaline earth metal atoms was varied to tune the physicochemical properties of the resulting BAe_3 system. Both basic systems (built of three identical substituents, such as BSr_3) and mixed systems (containing various substituents, such as $BCaMg_2$) were considered. The BAe_3 clusters feature low ionization energies (IEs) and a highly delocalized singly occupied molecular orbital (SOMO). Among them, the BBa_3 cluster was identified as having the lowest IE here (3.82 eV), exhibiting the superalkali characteristic, which is smaller than that of any alkali [3.89 eV (cesium atom)]. The BAe_3^+ thermodynamically stable closed-shell cations were shown to accommodate two electrons into their Rydberg orbitals, forming the double-Rydberg anions with electron binding energies in the 0.434–1.988 eV range. A mathematical model describing the dependence of IEs of BAe_3 clusters on their composition was developed. Different from the conventional formulation-assisted methodology, the quantitative structure–property relationship (QSPR) strategy predicts the reducing ability of a BAe_3 superalkali, where a suitable alkaline earth metal decreases the IE of the resulting BAe_3 cluster *via* the B–Ae and Ae–Ae electrostatic effects. Finally, the potential application of BAe_3 electron donors in the reduction of counterpart systems with low electron affinity (such as carbon dioxide or nitrogen molecules) was demonstrated. From the analysis of the binding energy between BAe_3 and the Y (Y = CO_2 and N_2) counterparts, as well as the charge transfer, and the geometry of BAe_3/Y systems, it follows that the resulting structures can be considered as either the $[BAe_3][Y]$ complexes or the BAe_3Y compounds. It is shown that the IE and the dipole moment of BAe_3 determine the stability and geometry of the resulting BAe_3/Y species. The lower IE and larger dipole moment promote the reactivity of BAe_3 and result in the formation of stable, strongly bound compounds. These findings highlight how the structure and stability of the BAe_3/Y systems can be tuned upon single atom substitution and can be used to bond and remove toxic molecules from the environment.

Received 30th July 2025,
Accepted 23rd September 2025

DOI: 10.1039/d5cp02913a

rsc.li/pccp

1. Introduction

Reducing agents play a crucial part in chemical synthesis.[1,2] Strong reductors have low ionization energies. Among the periodic table elements, alkali metal atoms exhibit the lowest ionization energies (5.39–3.89 eV). Superalkalis have even lower ionization energies than those of the alkali metal atoms. In 1982, Gutsev and Boldyrev introduced the simple formula ML_{k+1} to describe one class of superalkalis, where M is a *k*-valent electronegative central atom ligated with $k + 1$ alkali-metal atoms (L).[3] Typical examples of such superalkalis are FLi_2,[4,5] OLi_3,[6,7] and CLi_5.[8] The ML_{k+1} molecular system exhibits a high tendency to lose one valence electron, forming a very stable cation with the positive charges distributed over all the $k + 1$ alkali atoms (L). The existence of OL_3 (L = Li, Na, and K), ML_2 (M = F, Cl, Br, and I; L = Li, Na, and K), SLi_3, Li_3F_2, Li_2CN, and Na_2CN superalkalis has been confirmed by experiments.[9] Since the early 1980s, a lot of effort has been devoted to proposing alternative superalkali species, including polynuclear N_4Mg_6L (M = Li, Na, and K) superalkali species, alkali-metal coordinated crown ether complexes,[10] organic heterocyclic molecules,[11] superalkali molecules containing halogenoids,[12,13] organo-Zintl superalkalis,[14] and superalkalis with a boron atom acting as the central atom.[15,16] Despite these achievements, it is still desirable to obtain novel superalkali species, to seek even lower

[a] *Faculty of Chemistry, University of Gdańsk, Fahrenheit Union of Universities in Gdańsk, 80-308 Gdańsk, Poland. E-mail: celina.sikorska@ug.edu.pl*
[b] *Department of Physics, The University of Auckland, 38 Princes Street, Auckland 1010, New Zealand*

ionization energies. The boron-based superalkali design seems to be the most promising direction to obtain efficient reducers for CO_2 and N_2 activation.

Exploration of new superalkali species aims to provide reliable data and predictions of the use of such compounds as electron donors in the reduction of counterpart systems with low electron affinity, as well as the role they can play more generally in materials science.[1] The low ionization energies of superalkalis make them candidates for catalysts for N_2 and CO_2 conversion into ammonia and fuel, respectively.[17–20] By using the superalkalis as building blocks of cluster-assembled materials, we can achieve the functional features of atom-based materials (like conductivity or catalytic potential) while having more flexibility to achieve higher performance.[21–25] Superalkalis could be substituted for atoms as functional units because they potentially possess atomic-like functions (including redox activity).[1,22] To date, only a few superalkali-based bulk materials have been synthesized.[26,27]

Small isolated molecular clusters can serve as catalytic centres in single-cluster catalysis. In single-cluster catalysis, the metal clusters are not aggregated into larger particles or bulk materials, but rather, they exist as isolated entities, often stabilized on a support material (such as oxide or carbon supports). For instance, the triatomic ruthenic cluster supported by carbon nitride species (Ru_3/CN) has shown outstanding performance in the selective oxidation reaction of alcohols to aldehydes.[28] However, the controlled synthesis of supported atomic clusters is challenging, as stabilizing the precise numbers of atoms on the support in a rational manner is difficult. The synthetic methods to prepare supported metal clusters with precise numbers of atoms include a precursor-preselected approach,[28] host–guest strategy,[29] wet chemical reduction,[30] dendrimer-based technique,[31] and atomic layer deposition method.[32,33] The size of molecular clusters determines the fraction of surface atoms, which has a significant effect on both catalytic activity and selectivity. In supported atomic clusters, most of the metal atoms are exposed and available for the reactant molecules. As a result, supported atomic clusters exhibit much higher utilization efficiency in catalytic reactions compared to corresponding nanoparticles or single-atom catalysts.[33] Supported atomic clusters also possess unique electronic structures due to the orbital overlapping between metal atoms. The synergistic effect among metal atoms for boosting catalytic performances is uniquely distinct in supported atomic clusters containing two or more types of metal atoms.[34] With the development of synthesis and characterization, supported atomic clusters are expected to become a key area of research. Since the composition and structure of superalkali clusters can be tuned to optimize the selectivity and efficiency of the catalyst, designing and investigating this class of compounds for single-cluster catalysis applications holds great promise.

This contribution is aimed at designing superalkalis for redox applications and as building blocks for cluster-assembled materials. According to our recent results,[17] a superalkali with lower ionization energy should more easily transfer an electron to counterpart molecules (*e.g.*, carbon dioxide or nitrogen) compared to one with higher ionization energy. A promising direction for designing effective reductors is by utilizing boron-based molecules (such as BCa_3[35] or BLi_6[4]). Boron atoms have both empty and occupied atomic orbitals (in resemblance to the d orbitals of the gold atom[21]), which makes them capable of synergistically accepting and donating electrons. Thus, we decided to consider novel superalkali systems utilizing boron-based molecules. Specifically, our candidates were BAe_3 clusters (Ae = Be, Mg, Ca, Sr, and Ba). In these systems, we can change the type of electropositive atoms to tune the physicochemical properties of the resulting system. There are both basic (built of the identical three substituents, such as BSr_3) and mixed (containing various substituents, such as $BCaMg_2$) systems. Since alkaline earth elements (Mg, Ca, Sr, and Ba) are abundant and cheap,[36,37] using them to facilitate industrially relevant chemical transformations is prospective. Recently, we used alkaline earth metal atoms in superalkali design and proved that they can donate valence electrons to the central atom.[17] By using diverse alkaline earth metal ligands decorating the central boron atom, we were able to design superatoms with the desired ionization energy values. The studied superatomic systems with high thermodynamic stability and low ionization energy can act as reducing agents of carbon dioxide and nitrogen molecules.

2. Theoretical methods

2.1. Quantum chemistry methods

The second-order Møller–Plesset (MP2) perturbational method was employed with the Pople split-valence basis sets of triple zeta quality, 6-311+G(3df),[38] to optimize the geometry of $BAe_3^{0/\pm}$ (M = Be, Mg, Ca, Sr, and Ba) and BAe_3/Y (Y = CO_2 and N_2) ground states. For the relaxed structures, the vibrational frequencies were obtained at the same level of theory. The coupled-cluster method with single, double, and non-iterative triple excitations, CCSD(T), using the 6-311+G(3df) basis, was applied to estimate the final energies of the species at their MP2/6-311+G(3df) equilibrium geometries. The basis sets of Ahlrichs and coworkers' split valence and quadrupole zeta quality (Def2QZVP) were employed for strontium and barium atoms.[39,40] The above computations were carried out using the Gaussian 16 (Rev. C.01) software.[41]

In the next step, the reducing (ionization energy) and oxidizing (electron affinity) abilities of non-mixed and mixed BAe_3 (Ae = Be, Mg, Ca, Sr, and Ba) molecular clusters were evaluated. The adiabatic ionization energy (AIE) was estimated by subtracting the total electronic energies of the cation (E_{cat}) and neutral species (E_{neu}) at each equilibrium geometry ($r_{e,+}$ and $r_{e,0}$, respectively; eqn (1)). The adiabatic electron affinity (AEA) was calculated by subtracting the total electronic energies of the neutral (E_{neu}) and anionic species (E_{an}) at each equilibrium geometry ($r_{e,0}$ and $r_{e,-}$, respectively; eqn (2)). The vertical ionization energy (VIE, eqn (3)) and the vertical electron affinity (VEA, eqn (4)) values were obtained at the CCSD(T)/6-311+G(3df) level of theory at the MP2/6-311+G(3df) equilibrium geometries of the neutral species ($r_{e,0}$).

$$\mathrm{AIE} = E_{cat}(r_{e,+}) - E_{neu}(r_{e,0}) \quad (1)$$

$$\mathrm{AEA} = E_{neu}(r_{e,0}) - E_{an}(r_{e,-}) \quad (2)$$

$$\mathrm{VIE} = E_{\mathrm{cat}}(r_{\mathrm{e},0}) - E_{\mathrm{neu}}(r_{\mathrm{e},0}) \quad (3)$$

$$\mathrm{VEA} = E_{\mathrm{neu}}(r_{\mathrm{e},0}) - E_{\mathrm{an}}(r_{\mathrm{e},0}) \quad (4)$$

The adiabatic ionization energies (AIEs) and vertical electron affinities (AEAs) were calculated using the CCSD(T)/6-311+G(3df)//MP2/6-311+G(3df) approach and comprising zero-point energy corrections. The stabilities of $BAe_3^{0/\pm}$ systems were examined by obtaining their binding energies per atom (E_b) at the CCSD(T)/6-311+G(3df)+Def2QZVP level, defined as given in the following equations:

$$E_b(BAe_3) = \frac{[E(B) + 3 \cdot E(Ae) - E(BAe_3)]}{4} \quad (5)$$

$$E_b(BAe_3^+) = \frac{[E(B) + 2 \cdot E(Ae) + E(Ae^+) - E(BAe_3^+)]}{4} \quad (6)$$

$$E_b(BAe_3^-) = \frac{[E(B^-) + 3 \cdot E(Ae) - E(BAe_3^-)]}{4} \quad (7)$$

The binding energy (BE) values of the superalkali/Y systems (Y = CO_2 and N_2) were estimated at the CCSD(T)/6-311+G(3df)+Def2QZVP level of theory, eqn (8).

$$\mathrm{BE} = E_{\mathrm{superalkali/Y}} - E_{\mathrm{superalkali}} - E_{\mathrm{Y}} \quad (8)$$

The Multiwfn v.3.6 program was used for wavefunction analyses.[42,43] The frontier molecular orbitals were generated with the ChemCraft v.1.8 program,[44] and the contour values used in the plots were estimated with the OpenCubeMan rev.0.01[45] using a fraction of electron density equal to 0.8.

2.2. Quantitative structure–property relationship (QSPR) modeling

The designed BAe_3 clusters were split into a training set used for calibrating a QSPR model and a test set later used for evaluating the predictive ability of the developed QSPR equation. The QSPR modeling was performed following the recommendations by the Organization for Economic Co-operation and Development (OECD). In the OECD principles for the structure–property relationship approach, the accurately developed and validated model should meet the following five conditions: (i) a defined endpoint, (ii) an unambiguous algorithm, (iii) a defined applicability domain (AD), (iv) appropriate measures of goodness-of-fit, robustness, and predictivity and (v) a mechanistic interpretation, if possible.[46,47] The OECD principles are fulfilled by the developed QSPR model since it has a clearly described endpoint (adiabatic ionization energy) and the algorithm (a simple linear regression, SLR). In the SLR approach, the endpoint (y_i) is defined as the linear regression model of the most relevant descriptor used as a variable (x, eqn (9)):

$$y_i = b_0 + b_1 \cdot x \quad (9)$$

The next essential step of the model's development was to define its applicability domain. The applicability domain is a theoretical region restricted by the range of the endpoint and structural similarity between the compounds of interest, whereas the model predictions are the most reliable. In the present study, the structural applicability domain was verified by the leverage approach. The leverage values (h_i) were obtained as follows (eqn (10)):[48]

$$h_i = x_i^{\mathrm{T}}(X^{\mathrm{T}}X)^{-1}x_i \quad (i = 1, \ldots, n) \quad (10)$$

where x_i stands for the descriptor row-vector of the ith molecular cluster, x_i^{T} is the transpose of x_i, X is the descriptor matrix, and X^{T} is the transpose of X matrix. In the leverage approach, the critical leverage (h^*) is fixed at $3(m + 1)/n$ value, where n represents the number of compounds in the training set and m is the number of descriptors engaged in the correlation. The model's prediction is unreliable for a molecule whose leverage (h_i) exceeds the critical h^* value.[47] In contrast, when the leverage value of a compound is lower than the critical h^* value, the probability of accuracy between predicted and observed (experimental) values is as high as that for the compounds in the training set. The possibility of a compound being within the QSPR model's structural applicability domain can be verified for each new compound, and the only knowledge needed is the molecular structure information represented by the molecular descriptors selected in the QSPR model.

In the last step, the developed QSPR was validated by both internal and external validation. For the internal validation, the leave-one-out cross-validation method (LOO) was employed, and the model's robustness was assessed by the cross-validation coefficient (Q_{CV}^2) and the root mean square of cross-validation ($RMSE_{CV}$). The external validation of the model was conducted with an external test set composed of data not used to develop the prediction QSPR equation. The predictive ability of the model was defined by the external validation coefficient (Q_{EXT}^2) and the root mean square of prediction ($RMSE_{EXT}$). Statistics describing goodness-of-fit, robustness, and prediction ability of the QSPR model were obtained with the equations presented in Table S9.

3. Results

3.1. Geometry and thermodynamic stability of non-mixed and mixed BAe_3 clusters

We first optimized the lowest-energy structures of the non-mixed $BAe_3^{0/\pm}$ (Ae = Be, Mg, Ca, Sr, and Ba) clusters (Fig. 1 and 2), from which the adiabatic ionization energies of BAe_3 were estimated to be in the 3.818–6.830 eV range, exhibiting an alkali-like characteristic. As shown in Fig. 1 and 2, in the neutral non-mixed BAe_3 (Ae = Be, Mg, Ca, Sr, and Ba) clusters, the B central atom binds with three Ae substituents forming a pyramidal geometry of the C_{3v}-symmetry with the dihedral B–Ae_1–Ae_2–Ae_3 angle in the 39–65° range and decreases with an increase in the atomic radii of alkaline earth metal atoms. These findings are consistent with a previous study on triligated boron species,[35] validating the accuracy of the present theoretical level. Also, we found out that replacing Pople's split-valence triple-zeta basis set with standard sets of diffuse and polarization functions, 6-311+G(d), supplemented by three d-symmetry sets plus one f-symmetry set of polarization (*i.e.*, 6-311+G(3df)) leads to significantly better electronic stability estimation (Table S1 of the SI).

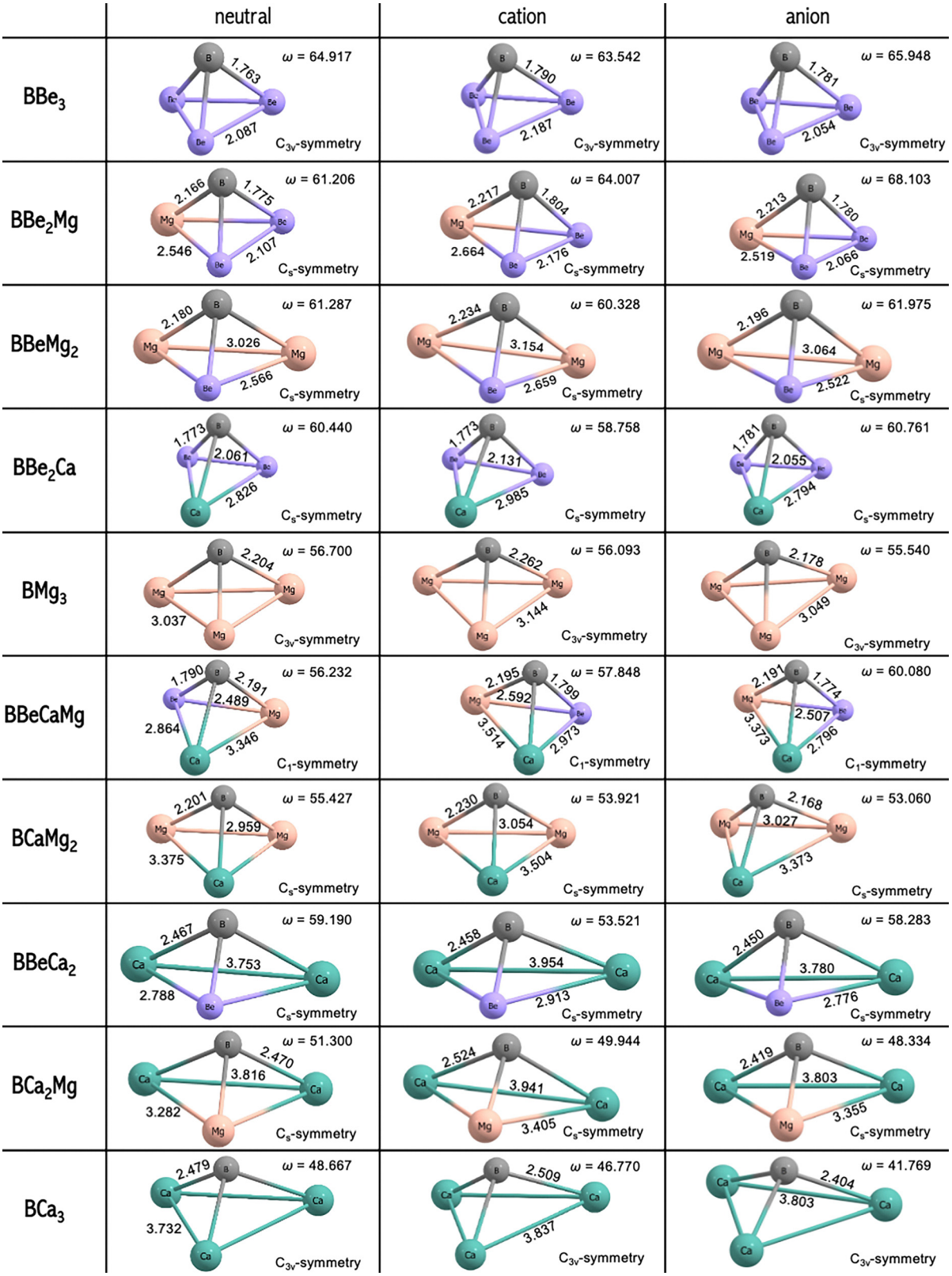

Fig. 1 The MP2(full)/6-311+G(3df) ground state structures of $BAe_3^{0/\pm}$ (Ae = Be, Mg, and Ca) species. Bond lengths in Å and dihedral B–Ae_1–Ae_2–Ae_3 angles (ω) in degrees. See Section S1 in the SI for higher energy isomers.

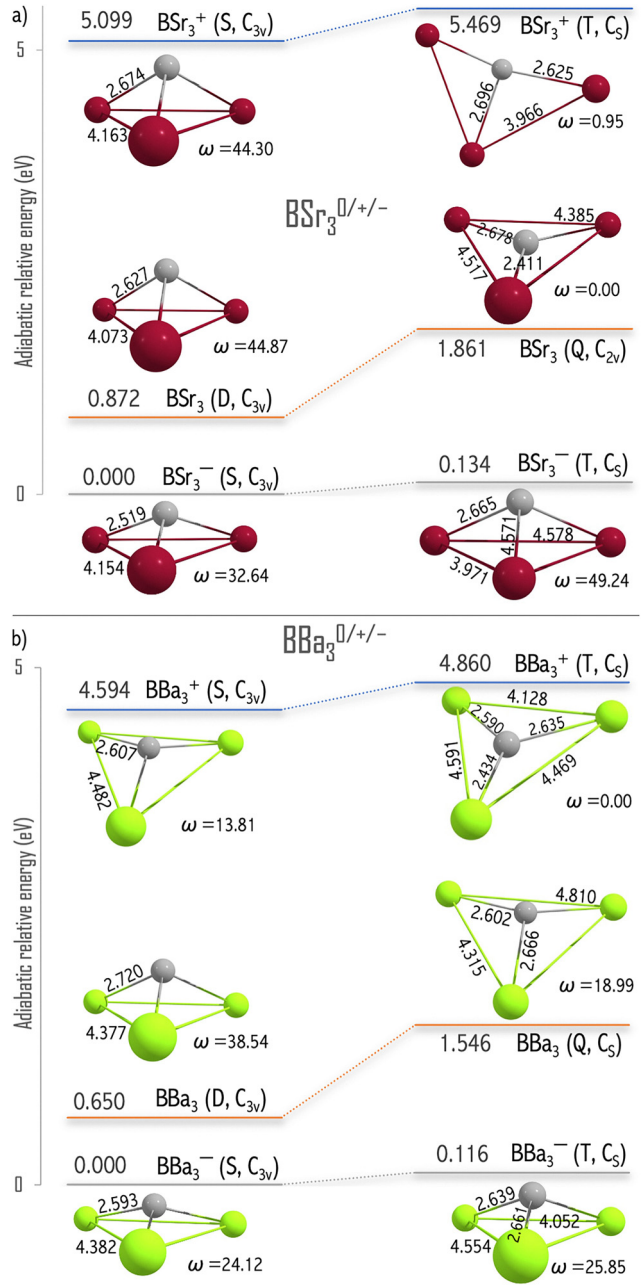

Fig. 2 The CCSD(T)(full)/6-311+G(3df)+Def2QZVP//MP2(full)/6-311+G(3df)+Def2QZVP energy diagrams showing adiabatic relative stability of (a) $BSr_3^{0/\pm}$ and (b) $BBa_3^{0/\pm}$ close- [singlet (S)] and open-shell [doublet (D), triplet (T), quartet (Q)] systems (with respect to the corresponding lowest energy anionic BAe_3^- singlet spin states, whose energies were taken as zero). Bond lengths in Å and dihedral B–Ae_1–Ae_2–Ae_3 angles (ω) in degrees.

A similar tendency was found in the case of another class of superatoms, superhalogens, where the performance of the MP2/6-311+(3df) and CCSD(T)/6-311+(3df) approaches assures a very high accuracy of the results (the deviations should not exceed 3%).[49]

The BAe_3 systems are thermodynamically stable due to electrostatic interaction between the electron-withdrawing boron atom and electropositive alkaline earth metals (electronegativity in the Pauling scale in the 0.89–1.57 eV range) as well as covalent-like interactions between alkaline earth atoms. The Be–Be (2.09 Å), Mg–Mg (3.04 Å), Ca–Ca (3.72 Å), Sr–Sr (4.07 Å), and Ba–Ba (4.38 Å) bonds of non-mixed BAe_3 clusters are near the bond lengths of homometallic bonding of M_2^{2+} cations (2.14, 2.91, 3.74, 4.23, and 4.69 Å respectively, as obtained at the same level of theory). The positive Gibbs free energies of the most probable dissociation channels (Table 1 and Table S2) and the non-mixed B_2Ae_6 dimer formation imply the thermodynamic stability of the BAe_3 clusters. Additionally, the binding energy per atom (E_b) covers the 0.73–1.44 eV range and decreases in the order BBe_3 (1.44 eV) > BBa_3 (1.02 eV) > BCa_3 (0.93 eV) > BSr_3 (0.87 eV), implying the influence of composition and size on the cohesion of the BAe_3 molecules.

To understand the regulation effect of the alkaline earth metal atoms on the redox properties of BAe_3 clusters, the global minima and low-energy isomers of selected mixed $BAe_3^{0/\pm}$ (Ae = Be, Mg, and Ca) clusters were optimized, which are shown in Fig. 1 and Fig. S1, respectively. In similarity to the non-mixed systems, mixed BAe_3 ground states reveal that the B central atom binds with three Ae atoms forming a pyramidal-like structure. Linear and flat isomers are higher in energy by 0.34–5.79 eV, Fig. S1. As shown in Fig. 1, the detachment/attachment of one electron does not alter the whole structural framework, the pyramidal-like geometry, of BAe_3. The ionic mixed $BAe_3^{\pm}$ (Ae = Be, Mg, and Ca) ground states feature the pyramidal-like geometry with the dihedral angle B–Ae_1–Ae_2–Ae_3

Table 1 Free enthalpies (ΔH_r^{298} in kcal mol^{-1}), entropies [ΔS_r^{298} in cal (mol K)$^{-1}$], and Gibbs free energies (ΔG_r^{298} in kcal mol^{-1}) of the BAe_3 → BAe_2 + Ae fragmentation reactions and the BAe_3 → $\frac{1}{2}B_2Ae_6$ dimer formation (at T = 298.15 K, p = 1 atm) obtained at the CCSD(T)/6-311+G(3df)+Def2QZVP level of theory for the BAe_3 (Ae = Be, Mg, Ca, Sr, and Ba) ground states. For the higher energy fragmentation channels (*i.e.*, BAe_3 → BAe + Ae_2, BAe_3 → BAe + 2Ae, and BAe_3 → B + 3Ae), see Section S4 in the SI)

Fragmentation path		ΔH_r^{298}	ΔS_r^{298}	ΔG_r^{298}
BBe_3 →	BBe_2 + Be	65.21	30.00	56.27
	$\frac{1}{2}B_2Be_6$	−2.32	−19.67	3.55
BBe_2Mg →	BBe_2 + Mg	44.38	25.70	36.72
	BBeMg + Be	90.41	28.61	81.89
$BBeMg_2$ →	BMg_2 + Be	52.13	26.20	44.32
	BBeMg + Mg	68.57	27.01	60.52
BBe_2Ca →	BBe_2 + Ca	56.48	25.03	49.02
	BBeCa + Be	66.89	29.49	58.09
BMg_3 →	BMg_2 + Mg	32.12	26.57	24.20
	$\frac{1}{2}B_2Mg_6$	−1.52	−17.93	3.82
BBeCaMg →	BBeCa + Mg	42.46	27.92	34.14
	BBeMg + Ca	78.09	26.36	70.23
	BCaMg + Be	81.37	28.31	72.93
$BCaMg_2$ →	BMg_2 + Ca	39.48	23.82	32.38
	BCaMg + Mg	64.48	47.69	50.27
$BBeCa_2$ →	BBeCa + Ca	50.13	27.32	41.99
	BCa_2 + Be	84.65	25.55	77.04
BCa_2Mg →	BCa_2 + Mg	60.70	23.91	53.57
	BCaMg + Ca	70.36	47.17	56.30
BCa_3 →	BCa_2 + Ca	65.11	25.41	57.54
	$\frac{1}{2}B_2Ca_6$	−1.63	−19.38	4.14
BSr_3 →	BSr_2 + Sr	38.03	28.94	29.40
	$\frac{1}{2}B_2Sr_6$	−2.27	−19.22	3.46
BBa_3 →	BBa_2 + Ba	39.43	28.71	30.88
	$\frac{1}{2}B_2Ba_6$	−2.47	−19.22	3.26

Table 2 Adiabatic ionization energy (AIE, in eV), vertical ionization energy (VIE, in eV), adiabatic electron affinity (AEA, in eV), and vertical electron affinity (VEA, in eV) values for the BAe_3 (Ae = Be, Mg, Ca, Sr, and Ba) ground states estimated at the CCSD(T)/6-311+G(3df)+Def2QZVP//MP2(full)/6-311+G(3df)+Def2QZVP level. The lowest vibrational frequencies (V_1, in cm^{-1}), HOMO–LUMO gaps (HL gap, in eV), and binding energies per atom (E_b, in eV) for the $BAe_3^{0/\pm}$ (Ae = Be, Mg, Ca, Sr, and Ba) ground states

Cluster	Symmetry point group	AIE	VIE	AEA	VEA	Neutral			Cation			Anion		
						V_1	HL gap	E_b	V_1	HL gap	E_b	V_1	HL gap	E_b
BBe_3	C_{3v}	6.830	6.884	1.988	1.973	450	6.589	1.44	431	8.461	2.05	468	5.057	2.05
BBe_2Mg	C_S	6.147	6.191	1.708	1.698	290	5.664	1.19	290	7.802	1.53	292	4.200	1.73
$BBeMg_2$	C_S	5.628	5.670	1.485	1.492	179	5.467	0.95	180	7.340	1.42	143	4.025	1.44
BBe_2Ca	C_S	5.570	5.608	1.437	1.447	274	4.948	1.32	247	6.907	1.43	270	3.240	1.80
BMg_3	C_{3v}	5.221	5.267	1.294	1.341	158	5.360	0.73	175	7.035	1.31	142	3.973	1.18
BBeCaMg	C_1	5.193	5.232	1.299	1.311	147	4.715	1.05	144	6.415	1.26	69	3.808	1.20
$BCaMg_2$	C_S	4.901	4.937	1.171	1.222	136	4.715	0.81	140	6.028	1.09	116	3.225	1.23
$BBeCa_2$	C_S	4.835	4.861	1.168	1.189	118	4.570	1.14	108	5.775	1.43	103	3.052	1.55
BCa_2Mg	C_S	4.643	4.677	1.080	1.131	111	4.453	0.88	113	5.536	1.22	96	3.101	1.27
BCa_3	C_{3v}	4.462	4.485	0.990	1.053	122	4.348	0.93	120	5.176	1.32	102	3.092	1.29
BSr_3	C_{3v}	4.033	4.107	0.809	0.939	82	4.149	0.87	76	4.759	1.23	69	3.808	1.20
BBa_3	C_{3v}	3.818	3.765	0.435	0.939	58	3.504	1.02	57	3.964	1.29	56	3.282	1.24

in the 48–68° range. The B–Ae and Ae–Ae bonds are in the 1.773–2.524 Å and 2.055–3.954 Å range, respectively, in resemblance to typical B–Ae and Ae–Ae bonds.[17,36]

The difference between the vertical and adiabatic values of ionization energy and electron affinity offers valuable insight into the structural changes in a molecule upon electron loss and gain, respectively. Our CCSD(T)/6-311+G(3df)//MP2/6-311+G(3df) results reveal that the difference between VIP and AIP does not exceed 0.074 eV for all BAe_3 clusters, see Table 2. These small energy differences are accompanied by the pyramidal-like geometry of the cluster being preserved upon the BAe_3^+ cation formation. Similarly, for most BAe_3 species, the difference between VEA and AEA is small, being about 0.063 eV or less, implying minor geometry modification upon electron attachment. However, for BSr_3 and BBa_3, notable differences between vertical and adiabatic electron affinities are observed (0.130 and 0.504 eV, respectively), which provoke substantial changes in the bond length of the corresponding anionic clusters, as illustrated in Fig. 2 and further analysed in the following section.

3.2. Double-Rydberg anions and their prospective in chemistry

The BAe_3 clusters have adiabatic electron affinity in the 0.435–1.988 eV range (Table 2) and are, therefore, able to form stable anions. The HOMO analysis allows us to classify them as the double-Rydberg (DR) anions.[50] These DR anions consist of a closed-shell cation core (*i.e.*, BAe_3^+ parent cation) plus two excess electrons described by Rydberg orbitals, Fig. 3. The B–Ae distances of BMg_3^- (2.178 Å), BCa_3^- (2.404 Å), BSr_3^- (2.519 Å), and BBa_3^- (2.593 Å) are shortened compared to those found for the corresponding non-charged species (by 0.084, 0.105, 0.108, and 0.127 Å, respectively) due to effective bonding of an additional electron, Fig. 1.[17] Moreover, the electron affinity of BAe_3 molecules strongly depends on the molecular size. In general, a smaller alkaline earth metal (with a smaller atomic mass) leads to a larger AEA, and this observation agrees with the mathematical model for the electron affinity of superatom prediction.[47] According to this mathematical model,[47] there is a strong relationship between electron affinity and the nature of the orbitals

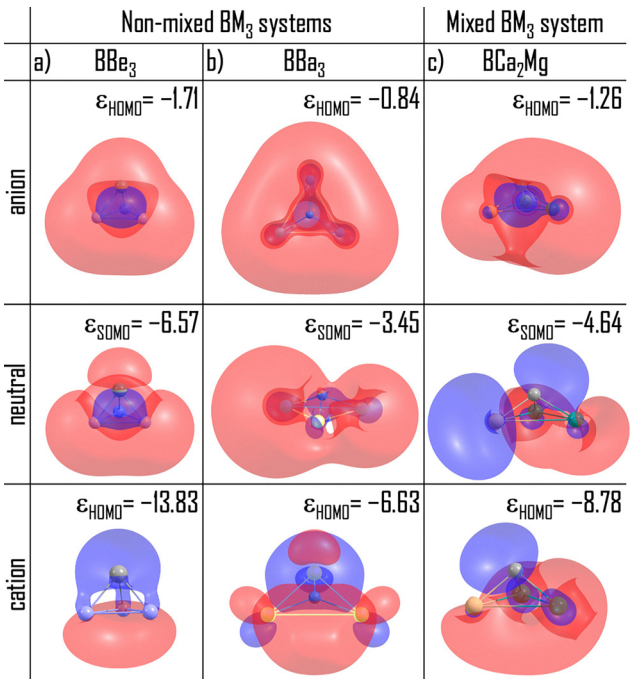

Fig. 3 The highest occupied molecular orbitals (HOMOs) and singly occupied molecular orbitals (SOMOs) of the ground state structures of representative (a) and (b) non-mixed and (c) mixed $BAe_3^{\pm}$ ions and their neutral BAe_3 parents, respectively. The HOMOs and SOMOs are plotted with a fraction of electron density (F_e) equal to 0.8 and their eigenvalues (ε_{HOMO} and ε_{SOMO}, respectively) are in eV. Contour values used in the plots were obtained with the OpenCubeMan rev.0.01 for F_e = 0.8.[45]

involved in the electron addition. Explicitly, the principal quantum number of the last electronic shell defines the size of the orbital and the energy of an additional electron. As the principal quantum number decreases, the orbital becomes smaller, and the electron density is closer to the nucleus. Also, as the principal quantum number of the last electronic shell decreases, the extra electron has lower potential energy and is, therefore, more tightly bound to the nucleus. Hence, introducing alkaline earth metals with a smaller principal quantum number of the last electronic shell results in an increase in electron affinity.

Based on the *ab initio* calculations, we demonstrated the ability of the MAe_3^+ closed-shell molecular cations to attach two electrons to their Rydberg orbitals to form double Rydberg anions. This class of anions was first experimentally confirmed in 1987 by Bowen and Eaton, who measured the electron binding energy of the NH_4^- anion to be 0.5 eV using a photodetachment experiment.[51] Later that year, Ortiz employed electronic structure calculations to predict that a tetrahedral closed-shell NH_4^+ cation surrounded by two electrons in a Rydberg-like orbital would have an electron binding energy of 0.42 eV.[52] Since then, numerous theoretical studies have been made to estimate the electron binding of various double Rydberg anions, including $H_3C–NH_3^-$, $NH_3NH_2^-$, NH_3OH^-,[53] and $N_4Mg_6M^-$ (M = Li, Na, and K).[17] We believe that the BAe_3^- double Rydberg anions designed and investigated here can exist at low temperatures in the gas phase (as an isolated species in the absence of any perturbations).

3.3. Electron localization function (ELF)

The ELF is a measure of electron localization and its usefulness for a superatomic system study is described elsewhere.[17,21,22] The normalized ELF = 1.0 represents perfect localization (*e.g.*, covalent bond and inner shell electrons), while the ELF = 0.5 corresponds to electron-gas-like probability. The topological analysis of the ELF leads to a partition into several ''basins'' that can be mapped to chemical concepts: core electrons, bonds, and lone pairs.[21] Fig. 4 shows valence basins located between the alkaline earth metal (Ae–Ae) atoms as well as boron and alkaline earth metal (B–Ae) atoms, indicating that the covalent-like bonds are formed between Ae–Ae and B–Ae atoms, respectively. A strong electron density delocalization ensures an enhanced electronic stability of the BAe_3 systems. As shown in Fig. 4, the electron delocalization (ELF = 0.5, coloured in green) reduces with the change of the ionization from an anion through neutral to a cation. Upon electron detachment, the electron delocalization reduces and valence electrons become more localized between atoms in the form of directional chemical bonds.

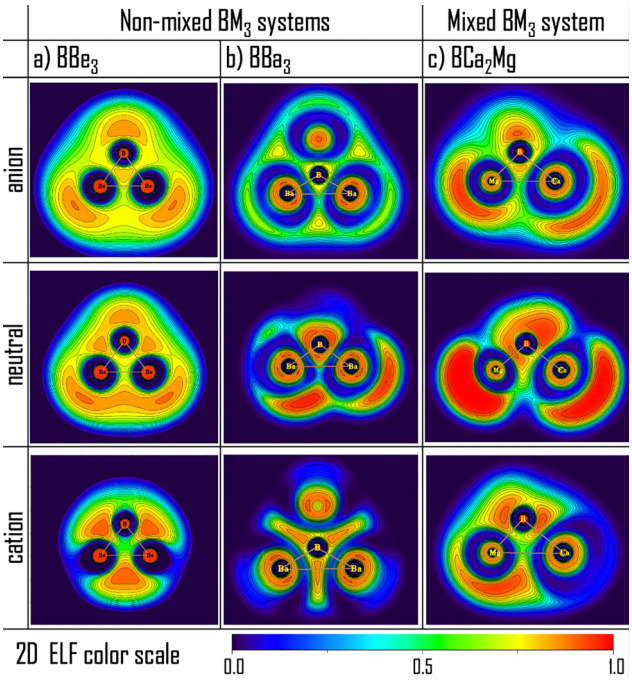

Fig. 4 Cut-plane electron localization function (ELF) plots of representative (a) and (b) non-mixed and (c) mixed anionic (top), neutral (middle), and cationic (bottom) BAe_3 clusters in the $B–Ae_1–Ae_2$ plane. The ELF plots were obtained with the Multiwfn v.3.8. software.[42,43]

3.4. Adiabatic ionization energies of BAe_3 clusters

Furthermore, to investigate whether the alkaline earth metal substitution process can enhance the capability of the clusters in detaching electrons, we calculated the AIE of clusters (Table 2). In Table 2, compounds are sorted by ascending molecular mass. In general, introducing larger alkali earth metals decreases the ionization energy, representing the electron-donor capability, of the BAe_3 clusters. Strikingly, BBa_3 was estimated to possess the lowest AIE value here (3.818 eV), exhibiting the superalkali characteristic, which is smaller than the lowest IE among alkali elements (Cs, 3.89 eV). We observed a monotonic AIE decrease with an increase in molecular size for all BAe_3 species.

The AIE depends on atomic mass. Different alkaline earth metal substituents affect the ionization energy of the BAe_3 system. We observed the most striking difference while comparing the $BBa_3/BSr_3/BCa_3/BMg_3/BBe_3$ set, as the replacement of three Ba atoms with three Sr, Ca, Mg or Be atoms leads to the ionization energy increase from 3.818 eV (BBa_3) to 4.033 eV (BSr_3), 4.462 eV (BCa_3), 5.221 eV (BMg_3), and 6.830 eV (BBe_3). The same pattern was found for the BCa_3 (4.462 eV)/BCa_2Mg (4.643)/$BBeCa_2$ (4.835 eV) and BCa_3 (4.462 eV)/$BCaMg_2$ (4.901)/BBe_2Ca (5.570 eV) series, where mixed substituents were introduced by replacing one or two Ca atoms with either Mg or Be atoms. This significant increase in the AIE value caused by atomic composition modification shows that the larger the atomic mass of the alkaline earth metal atom, the smaller the AIE of the resulting BAe_3 cluster. This implies that the electronic stability of the BAe_3 clusters (Ae = Be, Mg, Ca, Sr, and Ba) can be predicted from the atomic mass of the atoms comprising the superalkali-like systems. The lowest ionization energy values are expected for species containing electropositive substituents characterized by a large atomic mass. The above observation indicates that replacing a substituent in the superalkali-like system with a larger atom is highly favorable because it reduces electronic stability and enhances the reducing ability. This finding once again proves that suitable electropositive metals that the central atom is decorated with can regulate the electronic properties of the molecular cluster forming a superalkali.[3,17,21,54]

3.5. Superatomic electronic structure

The singlet spin state BAe_3^+ cations (Fig. 2) have a superatomic nature and follow the jellium model. According to the jellium model, the valence electrons are in quantized superatomic orbitals ($1S^2|1P^6|1D^{10}|2S^2$, $1F^{14}|2P^6$, $1G^{18}|\ldots$) distributed over the cluster. The superatomic clusters enhance their stability when the electronic shells are closed.[55] The BAe_3 neutral system has nine valence electrons ($3 + 3 \times 2$), thus one additional

electron than needed for the octet shell closure, in analogy to alkali atoms. The BAe_3 cluster can be seen as a doublet spin state open-shell superatomic structure (Fig. 2) with nine delocalized valence electrons. The thermodynamic stability accorded with the closure of the electronic shell meaning that BAe_3^+ cations have a $1S^2|1P^6$ electronic structure and their highest occupied molecular orbitals (HOMOs) have p-character, see Fig. 3. The closed-shell electron configuration of valence electrons determines the enhanced stability of the BAe_3^+ superatomic compounds.

The BAe_3^+ cations have large electronic stabilities. Their HOMO eigenvalues span the −13.82 eV (BBe_3^+, Fig. 3a) to −6.63 eV (BBa_3^+, Fig. 3b) range. The singly occupied molecular orbitals (SOMOs) of BAe_3 neutral parents are highly delocalized over the whole cluster, which ensures the reduction of repulsion interaction between electrons. Also, the highly diffused SOMO emphasizes that the outermost electron is loosely bound to the nuclei, giving rise to the low ionization energy. The SOMO character determines the reducing potential of BAe_3 clusters. We distinguish the difference in the SOMO nature of non-mixed and mixed systems. In the case of mixed clusters, the SOMO reveals the antibonding character with respect to the B–Mg (Fig. 3c) and bonding B–Be (Fig. S6d in the SI) interactions. In turn, the non-mixed cations have a bonding nature of all B–Ae interactions (Fig. 3a and b). The described alteration in the SOMO nature leads to symmetry breaking in mixed neutral clusters and subsequently decreases the electron stability and enhances the reducing potential of the resulting systems.

In the neutral superatom framework, it will be the delocalized valence electrons that determine the diamagnetic behaviour. Although a single unpaired electron would be expected to align parallel to the external applied field, the global ring current around the BAe_3 clusters results in substantial antiparallel alignment.[56] All BAe_3 species contribute to the diamagnetic susceptibility (with values ranging from -3.18×10^{-6} to -3.73×10^{-5} cm^3 mol^{-1}) with small paramagnetic contributions (ranking from 1.78×10^{-5} to 2.81×10^{-4} cm^3 mol^{-1}, Fig. S9 of the SI). The total magnetic susceptibility, derived as the sum of diamagnetic and paramagnetic contributions, remains weakly negative (from -4.51×10^{-6} to -1.95×10^{-5} cm^3 mol^{-1}), indicating an overall weak diamagnetism of the BAe_3 clusters. The observed diamagnetism is distinctive for superatoms with delocalized electrons.[56]

3.6. Natural bond orbital (NBO) analysis

As shown in Fig. 5a, the molecular size of the alkaline earth metals determines the ionization energy of the resulting clusters, which changes from the nonalkali (BBe_3, AIE = 6.830 eV) to the alkali (BBa_3, AIE = 3.818 eV) nature with the increment of alkaline earth metals' size. The interaction between boron and alkaline earth metal atoms has an electrostatic character. To check the charge distribution in the designed clusters, we performed the charge analysis using the natural bond orbital (NBO) approach. As can be seen from Fig. 5, the B atom gains electron density from Ae atoms, verifying the electron-withdrawing characteristic of the boron atom. The electrons of the Ae atoms enter either an antibonding (mixed clusters) or a bonding (mixed and non-mixed clusters) molecular orbital of the boron atom, and the energy of

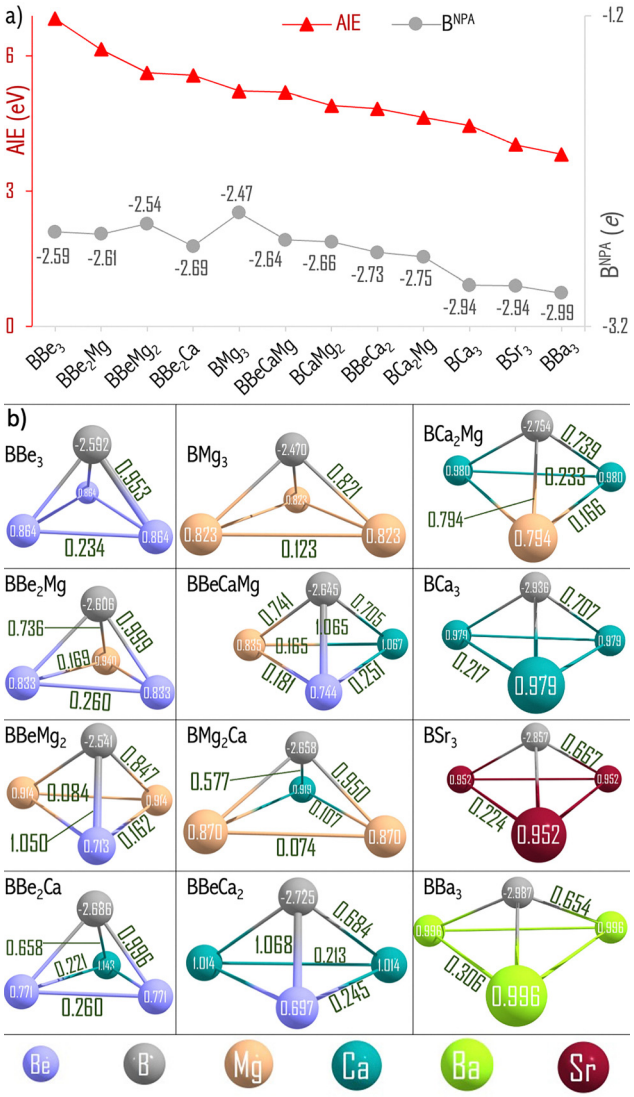

Fig. 5 (a) The adiabatic ionization energy (AIE, in eV) and natural charge on the boron atom by NBO analysis (B^{NPA}, in *e*) of the MP2(full)/6-311+G(3df) BAe_3 ground state structures. Clusters have been sorted by ascending molecular mass. (b) Natural atomic charges (in *e*) and Wiberg bond indexes (in green) by natural population analysis (NPA).

their bond in the BAe_3 molecule will be respectively lower or higher than in the isolated Ae atom. Such a continuous charge transfer (Fig. 5) between B and Ae atoms could enhance the electrostatic interaction between these boron and alkaline earth metal atoms, which produces BAe_3 clusters. The strength of the bond between B and Ae atoms in the BAe_3 clusters can be further evaluated by the Wiberg bond index (WBI, Fig. 5b) analysis. The relative B–Ae bond strength hierarchy given by WBI values in the non-mixed BAe_3 species is in the order B–Be (0.953) > B–Mg (0.821) > B–Ca (0.707) > B–Sr (0.667) > B–Ba (0.654), which implies that the B–Ae bond strength decreases as the atomic size of the alkaline earth metal increases. The stronger B–Be bond likely results from stronger covalent interactions, where boron's smaller atomic size allows for better overlap with the 2s orbital of beryllium, creating a stronger bond. Descending the group, the

larger ionic radii of Mg, Ca, Sr, and Ba result in poorer orbital overlap with boron, leading to a decrease in bond order.

The neutral BAe_3 clusters are open-shell systems with one unpaired electron (their ground electronic states are doublets, Fig. 2). These radical compounds have 34–89% spin density on the boron atom (Fig. S8 of the SI), due to its lower electronegativity in comparison with electropositive alkali earth metal substituents. The natural spin density localized on the boron atom in the non-mixed BAe_3 species gradually increases in the order 0.492 (BBe_3) < 0.825 (BMg_3) < 0.872 (BCa_3) > 0.893 (BSr_3) > 0.894 (BBa_3), which implies that the spin density on the B atom increases as the atomic size of the alkaline earth metal increases. Although the spin is largely localized on the B central atom, a significant part of the spin density is delocalized onto the Ae ligands. This is supported by natural spin density values on the Be (0.127–0.183), Mg (0.022–0.070), Ca (0.043–0.071), Sr (0.036), and Ba (0.035) atoms.

The linear-like trend in how the alkaline earth metal substitution modulates the AIE of BAe_3 clusters may be linked to the change in the frontier molecular orbital (MO) energies. It is well-known that the lowest unoccupied molecular orbital (LUMO) and highest occupied molecular orbital (HOMO) levels determine a species' ability to accept and donate electrons, respectively. Correspondingly, as shown in Fig. 6, the variation trend of the singly occupied molecular orbital (SOMO) levels of the BAe_3 clusters is in excellent agreement with that of the adiabatic ionization energy values. In addition, the HL gap of the cluster can be considered as one signature of enhanced stability and reduced reactivity. As shown in Fig. 6, the HL gap reduces as the molecular mass increases. Such a result of the HL gap is also consistent with the calculated AIE values.

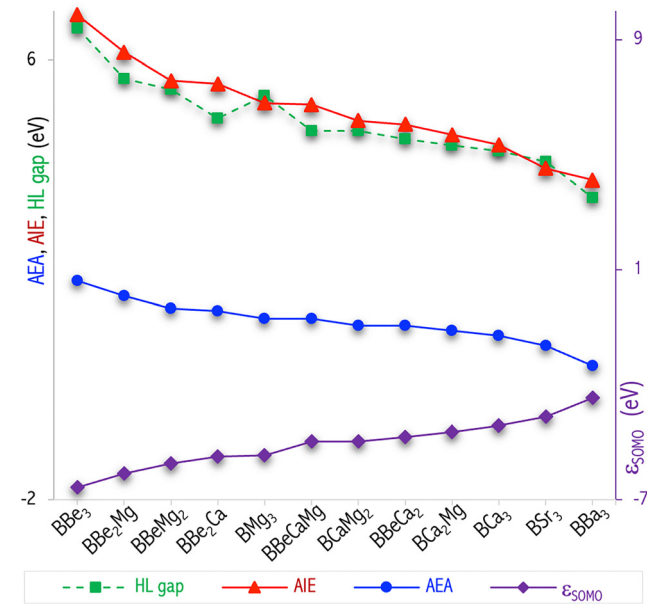

Fig. 6 The adiabatic electron affinity (AEA), adiabatic ionization energy (AIE), HOMO–LUMO gap (HL gap), and eigenvalue of singly occupied molecular orbital (ε_{SOMO}) of neutral BAe_3 clusters. Corresponding estimated data are listed in Table S3.

Consequently, the higher stability of the BAe_3 clusters results in their lower reducibility. This finding proves that suitable electropositive metals with which the central atom is decorated can regulate the electronic properties of molecular clusters forming a superalkali.

3.7. Empirical models for adiabatic ionization energy

To suggest an effective approach that could be used to predict the electron-donating ability of molecular clusters, we decided to develop mathematical models for ionization energy prediction. The developed models are described and discussed in Section S9 of the SI, while the most significant equations are provided in Fig. 7. Careful inspection of calculated AIE values (Fig. 7a) reveals that an accurate quadratic polynomial function can be fitted with a correlation coefficient value of 0.99 (R^2), which is AIE = $23.56 - 15.16{\cdot}x + 2.91{\cdot}x^2$, where x represents a decimal logarithm of molecular mass ($\log_{10} M$). Having such a relationship between the AIE and atomic properties, one can realize the precise regulation of the ionization energy of BAe_3 because the main feature of the superatomic systems is their atomic-precise tunability. For example, one can acquire the 6.83 eV AIE value of BAe_3 by synthesising a non-mixed beryllium-based molecular cluster. The electronic stability can be modulated *via* alkaline earth metal substitution. Replacing only one Be substituent in the BBe_3 system with larger Mg or Ca atoms is highly favorable because it enhances the reducing ability by 0.68 eV (BBe_2Mg) and 1.26 eV (BBe_2Ca), respectively. Such precise tunability of the electronic properties of the cluster upon structural modification represents a significant advantage in the superalkali construction strategy.

Similarly, well-fitting functions can be obtained by linking the cluster's ionization energy and a sum of ionization energies of constituent atoms as well as the Pauling electronegativity of atoms. The estimated quadratic AIE = $6.85 - 0.36x + 0.01x^2$ (where x represents the sum of atomic ionization energies, Fig. 7b) and linear AIE = $-1.80 + 1.19x$ (where x represents the sum of electronegativity, Fig. 7c) functions reveal R^2 equal to 0.98 and 0.99, respectively. Also, the sum of atomic radii allows us to predict the ionization energy of the BAe_3 cluster from the polynomial AIE = $22.02 - 3.53{\cdot}x + 0.17{\cdot}x^2$ ($R^2 = 0.93$, Fig. 7d) function. These findings demonstrate that the proposed substitution-based strategy for designing superalkali-like clusters works for the BAe_3 systems investigated here and can be applied to different superatomic systems. Thus, the proposed substituent modification-based strategy provides a potential methodology for constructing superalkalis for the chemical synthesis of atomically precise clusters, that is, applying suitable alkaline earth metals to synthesize stable molecular clusters having desirable ionization energy.

3.8. QSPR modeling

To further investigate the ability to predict the ionization energy of a superalkali cluster from its atomic features, we performed the quantitative structure–property relationship (QSPR) approach. The QSPR method mathematically links physicochemical properties with the structure of a molecule. The usefulness of this method has been confirmed for superatomic compounds (such as superhalogens).[47,57,58] The methodology applied is described

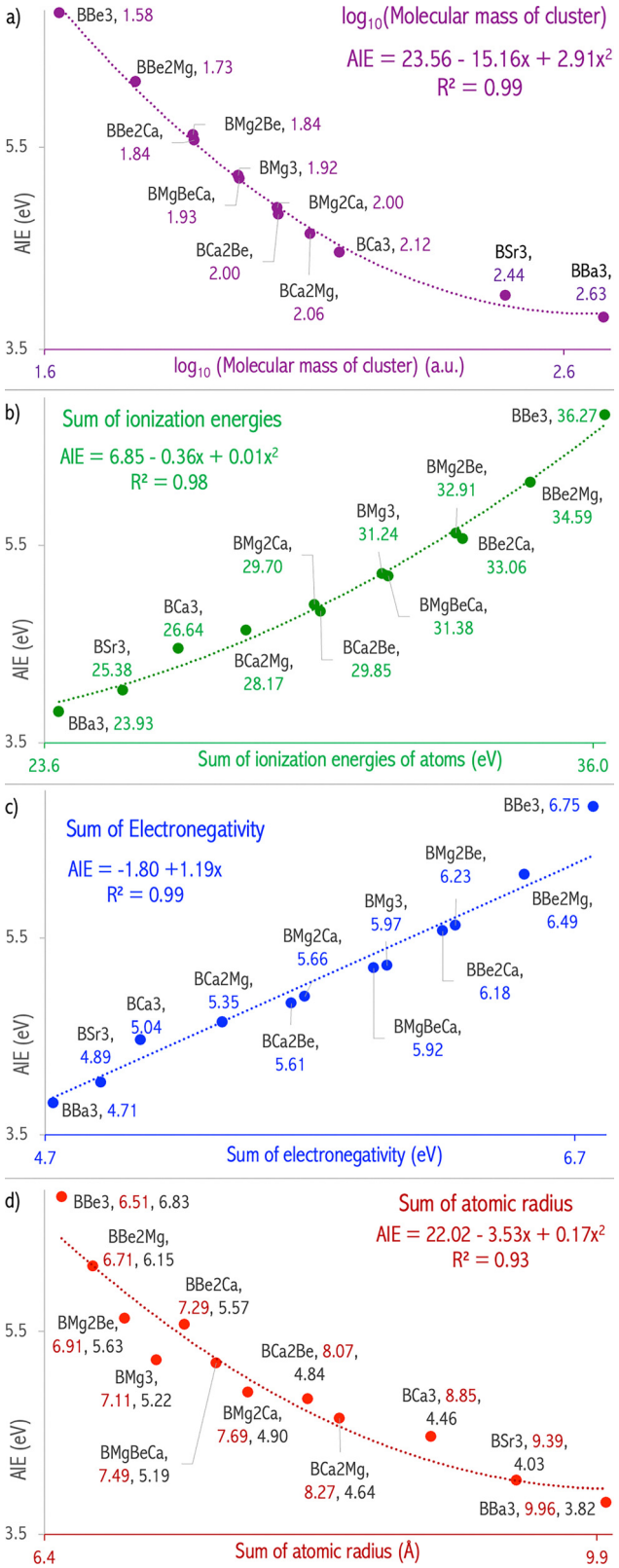

Fig. 7 Empirical models to predict adiabatic ionization energy of boron-based clusters from (a) decimal logarithm of molecular mass of a cluster ($\log_{10} M$), (b) sum of ionization energies of constituent atoms, (c) sum of Pauling electronegativity of constituent atoms, and (d) the sum of atomic radius.

elsewhere[47] and involved the following steps: (i) splitting the compounds into training and validation sets, (ii) calibrating a QSPR model, and (iii) internally and externally validating the model with the use of test and validation sets, respectively. In Table 3, the BAe_3 compounds were sorted in descending order of the AIE values, and then every second molecule was included in the test set (V), while the remaining compounds formed the training set (T). The above splitting algorithm leads to a uniform distribution of training and validation sets within the entire range of the AIE values. As a result, the BAe_3 clusters were separated into two independent subsets: a training set of 7 compounds to build a QSPR model and a test set of 5 compounds to evaluate the prediction ability of the developed model. The most significant QSPR model (eqn (11), where the descriptor represents the square of a sum of ionization energies of constituent atoms) exhibits determination coefficient (R^2), cross-validation determination coefficient (Q_{CV}^2), and external validation coefficient (Q_{EXT}^2) values close to 1, while the corresponding root mean square error values ($RMSE_C$, $RMSE_{CV}$, and $RMSE_{EXT}$, for their formulas see Section S10 in the SI), are both low and similar. Also, the visual correlation between the observed and predicted AIEs for the training (blue circles) and validation (red rectangles) sets illustrates the model's predictive capability (Fig. 8a).

$$\mathrm{AIE} = 1.468(\pm 0.167) + 0.004(\pm 1.801 \times 10^{-4}) \times \left(\sum_{i=1}^{nAt} \mathrm{IE}_i\right)^2 \quad (11)$$

$$R^2 = 0.990 \quad Q_{CV}^2 = 0.965 \quad Q_{EXT}^2 = 0.917$$

$$RMSE_C = 0.096 \quad RMSE_{CV} = 0.176 \quad RMSE_{EXT} = 0.168$$

In the next step, we used the leverage approach[59] to verify the chemical applicability domain of the developed model. The plot of the standardized residuals *versus* the leverage values (h_i, the Williams plot, Fig. 8b) confirmed that all BAe_3 molecules from the calibration and validation sets were established inside a squared area within ±3 standard deviation units and the leverage threshold ($h^* = 0.86$, green dashed line in Fig. 8b). The warning leverage, h^*, is fixed at $3(m + 1)/n$, where m is the number of descriptors involved in a QSPR equation and n is the number of compounds in the training set. In the Williams plot (Fig. 8b), neither training nor validation compounds are identified as X or Y-outliners, implying that their predictions are highly reliable. Thus, the QSPR model can be successfully applied to predict the reducibility of BAe_3 superalkali clusters and other untested superalkalis under the condition that the calculated h_i value for such a chemical structure is lower than the critical one ($h^* = 0.86$).

The interpretation of the physical meaning of the descriptor used in the developed QSPR model suggests that the ionization energy of the BAe_3 clusters (Ae = Be, Mg, Ca, Sr, and Ba) can be predicted from the sum of ionization energies of the atoms comprising the superalkali systems. The developed QSPR model implies that introducing more electron-donating substituents

Table 3 Adiabatic ionization energies estimated at the CCSD(T)/6-311++G(3df,3pd)+Def2QZVP level (AIE^{OBS}, in eV) and predicted by the QSPR model (AIE^{PRED}, in eV) for the BAe_3 (Ae = Be, Mg, Ca, Sr, and Ba) ground states. The differences between AIE^{OBS} and AIE^{PRED} are given by residual values (in eV). The sum of first ionization energies of the atoms comprising the BAe_3 cluster ($\sum_{i=1}^{nAt} IE_i$, in eV) and its square value ($\left(\sum_{i=1}^{nAt} IE_i\right)^2$ in eqn (11)). The compounds were split into a training set (T, later used for developing the QSPR model) and an external validation set (V, later used for evaluating the predictive ability of the model)

Compound	AIE^{OBS}	AIE^{PRED}	Residual	Sum of ionization energies $\left(\sum_{i=1}^{nAt} IE_i\right)$	$\left(\sum_{i=1}^{nAt} IE_i\right)^2$	Dataset splitting
BBe_3	6.830	6.673	0.157	36.27	1315.295	T
BBe_2Mg	6.147	6.202	−0.055	34.59	1196.468	V
$BBeMg_2$	5.628	5.754	−0.126	32.91	1083.266	T
BBe_2Ca	5.570	5.792	−0.222	33.06	1092.765	V
BMg_3	5.221	5.329	−0.108	31.24	975.688	T
BBeCaMg	5.193	5.364	−0.171	31.38	984.704	V
$BCaMg_2$	4.901	4.959	−0.058	29.70	882.268	T
$BBeCa_2$	4.835	4.993	−0.158	29.85	890.843	V
BCa_2Mg	4.643	4.608	0.035	28.17	793.549	T
BCa_3	4.462	4.275	0.187	26.64	709.530	V
BSr_3	4.033	4.017	0.016	25.38	644.297	T
BBa_3	3.818	3.734	0.084	23.93	572.836	T

decreases the ionization energy, representing the electron-donor capability, of the BAe_3 clusters. Strikingly, BBa_3 was estimated to possess the lowest AIE value here (3.82 eV), which is smaller than the lowest IE among alkali elements [3.89 eV (cesium atom)]. The developed mathematical model demonstrates that the electronic properties of molecular clusters forming the superalkali can be tuned upon an atom substitution within it.

To sum up, based on only one theoretical molecular descriptor, calculated exclusively from the molecular structures, we developed a QSPR model to estimate adiabatic ionization energies of the BAe_3 (Ae = Be, Mg, Ca, Sr, and Ba) superalkalis. The descriptor used, as a constitutional descriptor, does not depend on the conformation of a molecule or atom connectivity and only uses the atom information of the molecule for the calculation. The developed QSPR model, therefore, allows for the prediction of the ionization energy of a superalkali cluster based on the chemical composition of a molecule. The advantage of this approach lies in the fact that it requires only the knowledge of the chemical composition and does not require experimental quantities or quantum-mechanical computations. Hence, the developed QSPR model could provide reliable AIE values of superalkalis in the absence of theoretical characterization (*e.g.*, due to insufficient computer resources). Moreover, the QSPR model identifies the ionization energy of the atoms contributing the superalkalis as the most influential atomic property in determining the reducing capabilities of these superalkali clusters. We believe that the QSPR model and its interpretation, which we provided above, might be useful for theoretical and experimental chemists, especially those who design new materials with strong electron-donor features.

3.9. BAe_3 clusters as reducing agents for carbon dioxide activation

The BAe_3 clusters have low ionization energy and can be used as electron donors to reduce counterpart systems with low electron affinity. Hence, in the next step, we investigated the reducing effect of the BAe_3 clusters on the CO_2 molecule. Various binding sites for the CO_2 molecule on BAe_3 were extensively considered to determine the global minima of these complexes (see the SI for the low-energy isomers of BAe_3/CO_2). As shown in Fig. S10, S11 and Fig. 10, the BAe_3 interaction process leads to the deformation of the neutral CO_2 molecule, which changes from a linear geometry to a bent structure. The O–C–O valence angle reduces from linear to 110–133° upon the interaction with BAe_3, exhibiting its bent form. This implies that the interaction between BAe_3 and CO_2 is relatively strong. Additionally, in the BAe_3/CO_2 species (Fig. S10 and S11), the CO_2 subunit exhibits the bridging mode, where either the oxygen atom binds with alkaline earth metal or the carbon atom binds with Ae or B atoms, forming a covalent-like bond. Next, the binding energies (BEs, eqn (8)) of the CO_2 molecule onto the BAe_3 neutral clusters were explored to elucidate the interaction strength between the CO_2 molecule and a BAe_3 cluster (Fig. 9), which can also be used to estimate the stability of these interacting species. Since an effective catalyst must bind intermediates strongly enough to activate them, yet weakly enough to allow product release, the magnesium-based BAe_3 clusters emerge as promising candidates for CO_2 activation (the interaction strength is below 1 eV). The NBO charge transfer from the Mg-based BAe_3 clusters to the CO_2 molecule $\left(Q_{CO_2}^{NBO}\right)$ is from 0.88*e* (BBe_2Mg/CO_2) to 0.95*e* (BCa_2Mg/CO_2), which exceeds those gained by the CO_2 molecule from Li_3F_2 (0.63*e*),[60] C_5NH_6 (0.77*e*),[61] N_4Mg_6Li (0.80*e*),[17] N_4Mg_6Na (0.80*e*),[17] N_4Mg_6K (0.81*e*),[17] NLi_4 (0.85*e*),[62] OLi_3 (0.88*e*),[62] $B_9C_3H_{12}$ (0.89*e*),[61] $Mn(B_3N_3H_6)_2$ (0.90*e*),[61] and FLi_2 (0.90*e*).[62] The $Q_{CO_2}^{NBO}$ of the remaining BAe_3/CO_2 systems exceeds 1.25*e*, comparable to that observed in the Al_3/CO_2 complex (1.26*e*).[61] As shown in Fig. 9, the estimated BE values approach −3.21 eV, which implies a larger intermolecular interaction than those of the N_4Mg_6M/CO_2 (M = Li, Na, and K) species (BE values from −1.64 to −1.57 eV as obtained at the CCSD(T)/6-311+(3df) level[17]). Such large BE values probably stem from the

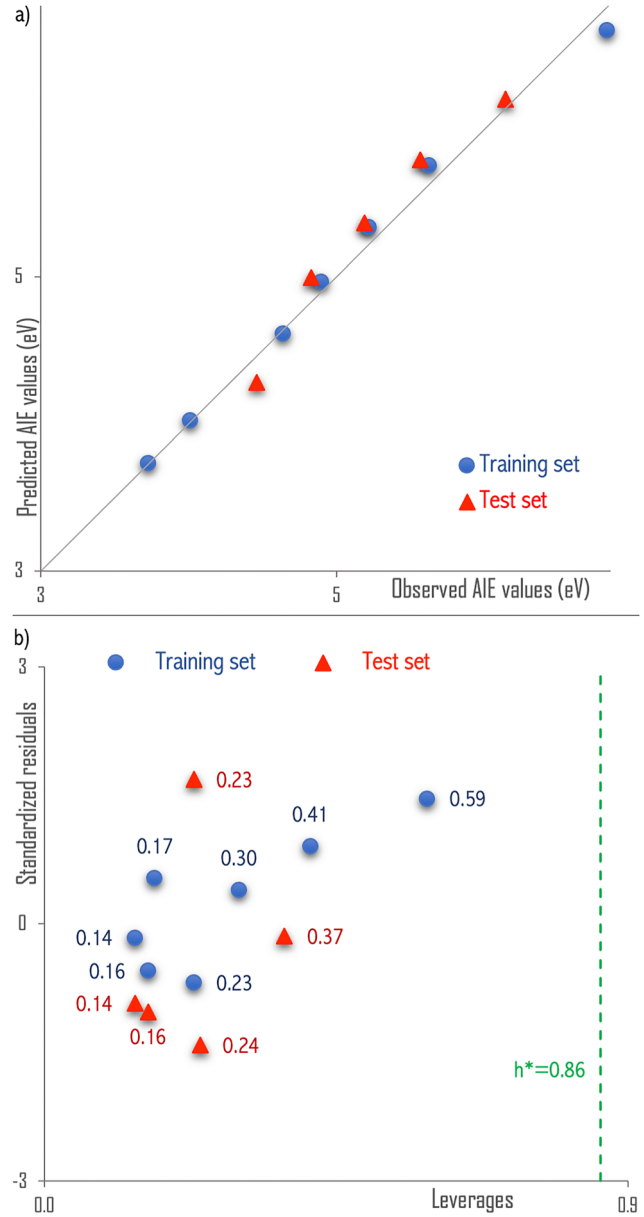

Fig. 8 (a) The plot of observed *vs.* predicted AIEs (in eV). (b) The Williams plot of the developed QSPR model. The Williams plot compares the leverage values (h_i, eqn (S1)) and standardized cross-validated residual values (AIE_{obs}–AIE_{pred_cv}). The green dashed vertical line corresponds to the leverage threshold (h^* = 0.86). The leverage threshold is defined as $h^* = 3(m + 1)/n$, where m is the number of descriptors involved in a QSPR equation and n is the number of compounds in the training set.

C–B, C–Ae, and O–Ae bridging modes, the charge transfer from the superalkali to carbon dioxide, and indicate the high stability of these BAe_3/CO_2 systems as well.

3.10. The role of the singly occupied molecular orbital (SOMO) in stabilizing the anionic form of carbon dioxide

A superalkali, acting as an electron donor, facilitates the reduction of carbon dioxide. The singly occupied molecular orbital (SOMO) of representative BMg_3/CO_2 species is mainly contributed by atomic orbitals of the carbon dioxide counterpart, rather than the BMg_3 cluster, as would be expected in a charge transfer $[superalkali]^+[CO_2]^-$ compound.[17] This observation implies a reduced form of carbon dioxide in the superalkali/CO_2 chemical system. The visualized HOMO and SOMO of CO_2 and CO_2^-, respectively, shown in Fig. 10 illustrate how the molecular structure alters upon the attachment of an excess electron. The neutral carbon dioxide molecule adopts a linear geometry, with its p-type HOMO and HOMO − 1 orbitals consisting of lone pair electrons of oxygen atoms (Fig. 10e). Upon gaining an additional electron, the point group of CO_2 changes from $D_{\infty h}$ to C_{2v}. The excess electron occupies the σ* antibonding orbital of carbon dioxide, and the hybridization of the carbon atom shifts from sp to sp^2-like as it accepts the electron, transforming into the CO_2^- anion. This change in hybridization triggers a bending of the carbon dioxide structure resulting in a CO_2^- anion (Fig. 10d).[61] In the BMg_3/CO_2 compound (Fig. 10c), the SOMO resembles the SOMO antibonding orbital of the CO_2^- anion (Fig. 10d). The HOMO − 1, HOMO − 2, and HOMO − 3 orbitals resemble the three highest occupied molecular p-type orbitals of the BMg_3^+ cation. Since CO_2 adopts a bent structure upon electron transfer or due to its interaction with the electrons of the metal atom (Fig. 10c),[17,61] the electron is transferred from a Rydberg-like orbital of open-shell BMg_3 cluster (Fig. 10a) to the σ* antibonding LUMO of carbon dioxide (Fig. 10e) to form the $[BMg_3]^+[CO_2]^-$ ionic compound.

As demonstrated above, the carbon dioxide moiety undergoes significant geometry relaxation upon interaction with the BAe_3 cluster to form the resulting BAe_3/CO_2 compound. Specifically, the structural changes in CO_2 upon interaction with the BAe_3 superalkali molecule convert its linear geometry toward the bent structure of CO_2^- anion. Although the final anionic structure of carbon dioxide is not entirely achieved in the superalkali/CO_2 product, this observation indicates the electron density donation, which takes place when a superalkali combines with a CO_2 molecule.

3.11. The mechanism of the CO_2 activation

The activation of the carbon dioxide molecule upon its interaction with a superalkali can be explained by choosing one representative system and determining the eventual kinetic (*i.e.*, activation) barrier that must be overcome to create the resulting $[superalkali]^+[CO_2]^-$ ionic compound. We decided to investigate the process by assessing the energy change that accompanies the reaction of substrates (superalkali and CO_2), leading to the creation of the CO_2^- anion for an arbitrarily chosen BMg_3/CO_2 system. While analyzing the energy profile for the BMg_3 + CO_2 → $[BMg_3]^+[CO_2]^-$ process, the excess electron must be assigned to BMg_3 rather than to CO_2 (for the separated BMg_3 and CO_2 systems) due to the considerably larger electron affinity of the BMg_3 cluster (AEA = 1.312 eV). Indeed, as indicated by the localization of the singly occupied molecular orbital, the additional electron is in the vicinity of the BMg_3 species (as depicted in Fig. 11). The part of the excess electron density gets transferred to the CO_2 subunit as the initially distant CO_2 approaches BMg_3 to form the $[BMg_3]^+[CO_2]^-$ ionic system (see Fig. 11 where

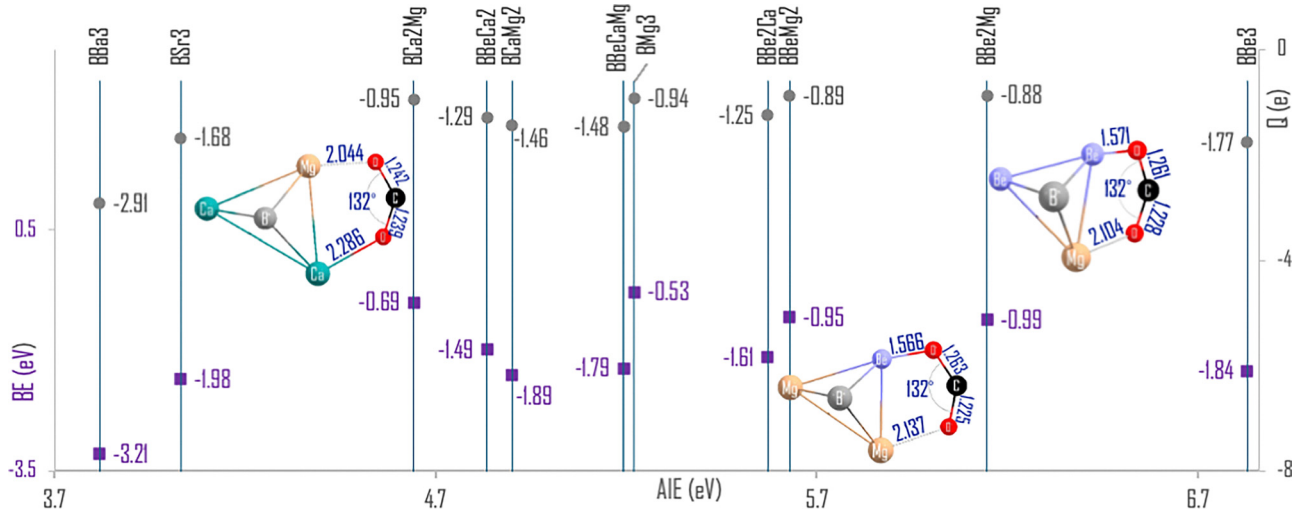

Fig. 9 The influence of the adiabatic ionization energy (AEA, in eV) on the binding energy (BE in eV) and charge flow ($Q_{CO_2}^{NBO}$ between the superalkali and CO_2). The ground states of representative magnesium-based complexes (*i.e.*, BCa_2Mg/CO_2, $BBeMg_2/CO_2$, and BBe_2Mg/CO_2) are also provided.

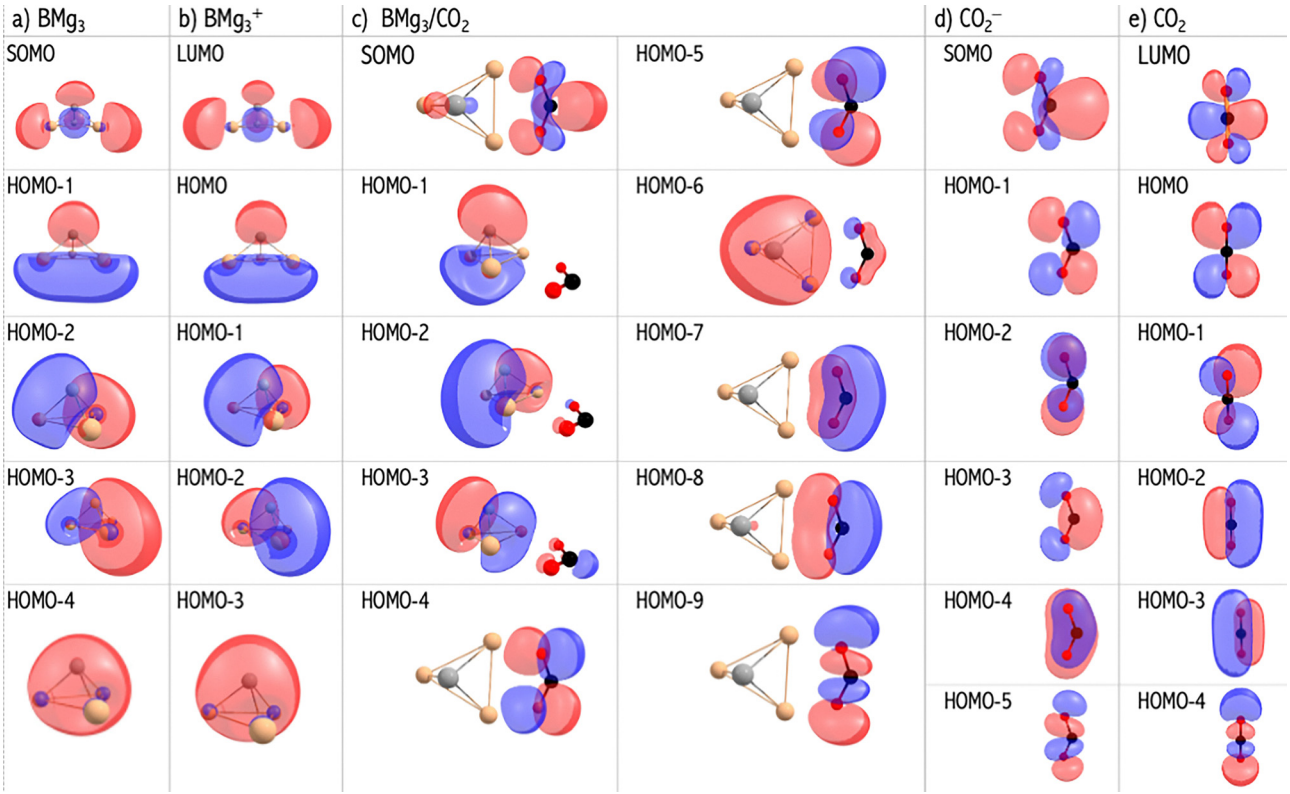

Fig. 10 The molecular orbitals of (a) the BMg_3 cluster, (b) BMg_3 cation, (c) BMg_3/CO_2 compound, (d) CO_2^- anion, and (e) CO_2 molecule. The complete active space self-consistent field method (CASSCF) was used to obtain molecular electronic structures.

also the SOMOs for the equilibrium $[BMg_3]^+[CO_2]^-$ structures are shown). The energy gradually decreases as the CO_2 molecule approaches the neutral BMg_3 cluster and there is no barrier that must be surmounted. Such barrierless behaviour is characteristic of gas-phase reactions involving radical species, where long-range capture interactions dominate the dynamics.[63] Since the energy of the separated BMg_3 radical and CO_2 molecule is significantly larger (by *ca.* 0.54 eV) than the energy of the $[BMg_3]^+[CO_2]^-$ ground state, and given that the $BMg_3 + CO_2 \rightarrow [BMg_3]^+[CO_2]^-$ process is predicted to be barrier-free, one may expect the $[BMg_3]^+[CO_2]^-$ ionic system to be created spontaneously in the gas phase (whenever CO_2 molecules find themselves in the vicinity of BMg_3 clusters).

The above observation implies that the strong reducing ability of a superalkali system makes it possible to activate

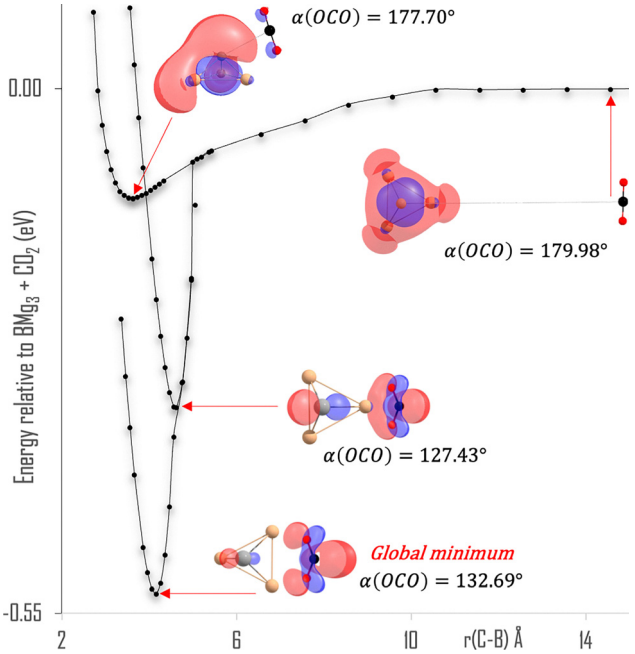

Fig. 11 The CCSD(T)/6-311++G(3df,3pd) energy profiles for the formation of the $[BMg_3]^+[CO_2]^-$ compound according to the BMg_3 + CO_2 → $[BMg_3]^+[CO_2]^-$ reaction. The relative energies are obtained in relevance to the sum of energies of isolated fragments [BMg_3; CO_2]. The singly occupied molecular orbitals (SOMOs) holding the excess electron are depicted for the structures corresponding to r = 4.060 Å (global minimum), r = 4.564 Å (local minimum), and r = 14.564 Å.

carbon dioxide by electron density transfer from a BAe_3 cluster to the CO_2 molecule and form its anionic CO_2^- form. Moreover, the binding strength can be modulated by the alkaline earth metal substitution in the BAe_3 cluster (Fig. 9). The precise control of the binding strength of the carbon dioxide on a molecular cluster is essential for its subsequent transformation into valuable chemicals.

3.12. BAe_3 clusters as reducing agents for nitrogen activation

To further testify to the chemical applicability of the designed molecular clusters, the nitrogen molecule activation was investigated. Fig. 12 illustrates the equilibrium geometries of the BAe_3/N_2 systems. The comparable energy of the two geometrically stable BMg_3/N_2 isomers (*i.e.*, not exceeding 0.1 eV) and the relatively long lifetime of the BMg_3/N_2 local minimum (τ = 62.63 s, see Section S13 in the SI) indicate that the interchange between these structures is probably rapid at the temperatures used experimentally. The binding energy of the BAe_3/N_2 ground states was calculated to span the range from −0.02 eV (BMg_3/N_2) to −1.92 eV (BCa_3/N_2), and the N_2 activation process seems to be an exothermic process for all systems. The BBe_3, BMg_3, and BSr_3 non-mixed and $BCaMg_2$ and $BBeCa_2$ mixed clusters form stable $[BAe_3][N_2]$ complexes in which N_2 and pyramidal-like BAe_3 subunits can be distinguished. In turn, the remaining BAe_3 clusters form strongly bound BAe_3N_2 compounds in which the pyramidal-like geometry of the BAe_3 cluster has not been preserved. While BCa_3/N_2 was computed at the PBE0/6-311+G(3df) level to be a pyramidal-like BCa_3 structure linked with a N_2 molecule through four Ca–N bonds and one B–N *via* an end-on pattern,[35] the calculations at the MP2(full)/6-311+G(3df) level

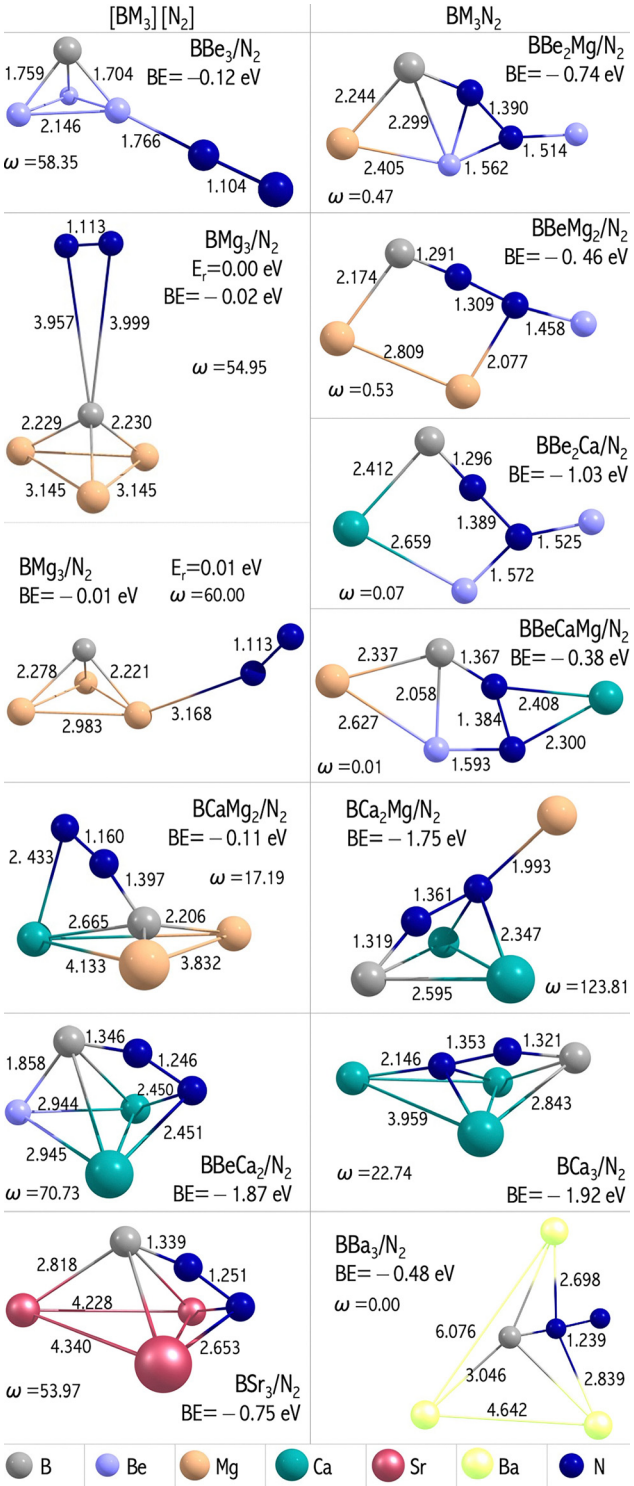

Fig. 12 The MP2/6-311+G(3df)+Def2QZVP ground states of $[BAe_3][N_2]$ and BAe_3N_2 (Ae = Be, Mg, Ca, Sr, and Ba) systems. The CCSD(T)/6-311+G(3df)+Def2QZVP//MP2/6-311+G(3df)+Def2QZVP binding energy (BE, in eV). Bond lengths in Å and dihedral B–Ae_1–Ae_2–Ae_3 angles (ω) in degrees. See Section S12 in the SI for higher energy isomers.

instead show a planar structure with a bent CO_2 structure inside a triangle formed by three alkaline earth atoms. Like the case in N_4Mg_6M/N_2,[17] the stability of BAe_3/N_2 (Ae = Be, Mg, and Sr) continuously increases, accompanied by the enhancement of the reducing strength of the non-mixed superalkali cluster. Additionally, the interaction strength depends on the superalkali cluster size. In smaller clusters (such as BMg_3), the outermost electron is more tightly bound by the nuclei, giving rise to lower reactivity of the cluster (BE = −0.02 eV). The interaction energy increase is naturally accompanied by enhanced charge transfer between the superalkali and N_2 subunits. As shown in Fig. 12, the largest charge flow (of 2.75*e*) has been observed for the strongest bound BCa_3/N_2 compound (BE = −1.92 eV). Remarkably, the N–N bond elongates from 1.113 Å (N_2 isolated neutral molecule) up to 1.389 Å (Fig. 12) upon the interaction with the BAe_3 cluster, exhibiting its anionic form. Upon nitrogen gaining one or two electrons, the N–N bond elongates from 1.113 Å (N_2 singlet spin state) to 1.192 Å (N_2^-) or 1.225 Å (N_2^{2-} triplet spin state), respectively, as obtained at the MP2/6-311+G(3df) level. The relatively low second ionization energy of the BAe_3 cluster (AIE2 in Fig. 14a) makes it possible to transfer two electrons from the superalkali to the nitrogen molecule. Consequently, in all BAe_3N_2 compounds, N_2 is in its dianionic state, which is confirmed by the NBO charge on the N_2 fragment (Fig. 14c) and N–N distances (Fig. 12). The above observation implies that the BAe_3 clusters have a strong reducing ability and can be used for nitrogen molecule activation.

The reduction of the nitrogen molecule by a superalkali has been assessed for an arbitrarily chosen BSr_3/N_2 system. While analyzing the counterpoise-corrected energy profile for the $BSr_3 + N_2 \rightarrow [BSr_3]^+[N_2]^-$ process, the excess electron is in the vicinity of the BSr_3 species (as depicted in Fig. 13). The part of the excess electron density gets transferred to the N_2 subunit as the initially distant nitrogen molecule approaches the BSr_3 superalkali to form the $[BSr_3]^+[N_2]^-$ ionic system (see Fig. 13 where also the SOMOs for the equilibrium $[BSr_3]^+[N_2]^-$ structures are shown). The BSr_3/N_2 system undergoes a decrease in energy as the fragments come together into the $[BSr_3]^+[N_2]^-$ ground state. However, upon nearing each other, the system temporarily stabilizes at a local minimum, characterized by a higher energy (by 0.357 eV) than that of the isolated fragments. This suggests that the fragments are interacting but not in the most stable configuration. Due to a sufficiently long lifetime (of 4.88 s, see Section S13 in the SI), the BSr_3/N_2 local minimum can serve as a metastable trap for intermediates under standard conditions used in the simulations (gas phase and room temperature). As the reaction progresses, the system continues to evolve, eventually reaching the global minimum of 2.191 eV lower in energy than the isolated fragments. The global minimum represents the most stable and energetically favourable state, with the local minimum acting as an intermediate step along the reaction path.

The variation tendency of the regulation effect of the alkaline earth metal atoms on the BAe_3/N_2 reaction products can relate to the change of the dipole moment (μ) upon the metal atom substitution, with a larger dipole moment promoting the reactivity of a BAe_3 cluster and forming stable, strongly bound

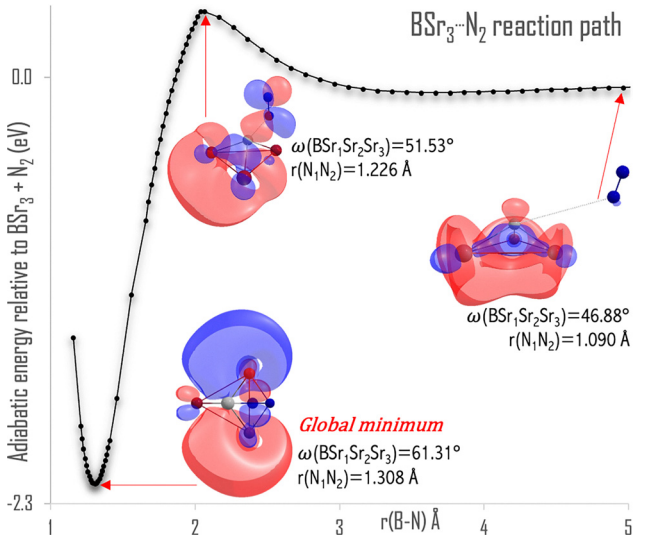

Fig. 13 The BSSE-corrected adiabatic energy profiles for the formation of the $[BSr_3]^+[N_2]^-$ compound according to the $BSr_3 + N_2 \rightarrow [BSr_3]^+[N_2]^-$ reaction. The relative energies are obtained in relevance to the sum of energies of isolated fragments [BSr_3; N_2]. The singly occupied molecular orbitals (SOMOs) holding the excess electron are depicted for the structures corresponding to *r* = 1.302 Å (global minimum), *r* = 1.965 Å (local minimum), and *r* = 4.965 Å. The basis set superposition error (BSSE) has been accounted for by using the counterpoise correction method.

BAe_3N_2 compounds. Hence, as shown in Fig. 14b, the variation trend of the dipole moments of the BAe_3 clusters agrees with that of the interaction energies for the BAe_3/N_2 systems. The dipole moment of the molecular cluster can be considered as one signature of reduced stability and enhanced reactivity. As illustrated in Fig. 14b, the BBeCaMg/N_2 (μ = 3.03 Debye) species is more stable (BE = −0.38 eV) than its neighbouring species, *i.e.*, BMg_3/N_2 (μ = 1.80 Debye, BE = −0.02) and $BCaMg_2/N_2$ (μ = 1.88 Debye, BE = −0.11 eV). Such a result of the dipole moment is also consistent with the calculated charge flow $\left(Q_{N_2}^{NBO}\right)$ values (Fig. 14c). Thus, the above findings demonstrate that the properly chosen BAe_3 clusters can significantly enhance the stability of BAe_3/N_2 species to transform the N_2 molecule into its activated ionic form.

The interaction of BAe_3 clusters with the N_2 molecule is characterized by the charge transfer from the BAe_3 superalkali to N_2, resulting in the formation of [superalkali][N_2] complexes. For example, the N_2 molecule interacts with the N_4Mg_6M (M = Li, Na, and K) superalkalis, forming complexes with binding energies of approximately 0.04 to 0.11 eV, accompanied by hardly any charge flow between interacting subunits ($Q_{N_2}^{NPA}$ up to 0.02*e*). Utilizing stronger reducing agents (whose ionization energies diminish by 4.4 eV) allowed us to reduce the nitrogen molecule. The nitrogen molecule activation was possible by the low ionization energy of the BAe_3 superalkali, with a smaller ionization energy promoting the transfer of an electron to N_2. The $Q_{N_2}^{NPA}$ of BSr_3/N_2 reads 0.75*e* which exceeds those gained by N_2 from N_4Mg_6Li (0.02*e*),[17] N_4Mg_6Na (0.02*e*),[17] N_4Mg_6K (0.02*e*),[17] NLi_4 (0.02*e*),[64] OLi_3 (0.01*e*),[64] and FLi_2 (0.7*e*).[64] The transition metal nitride complexes

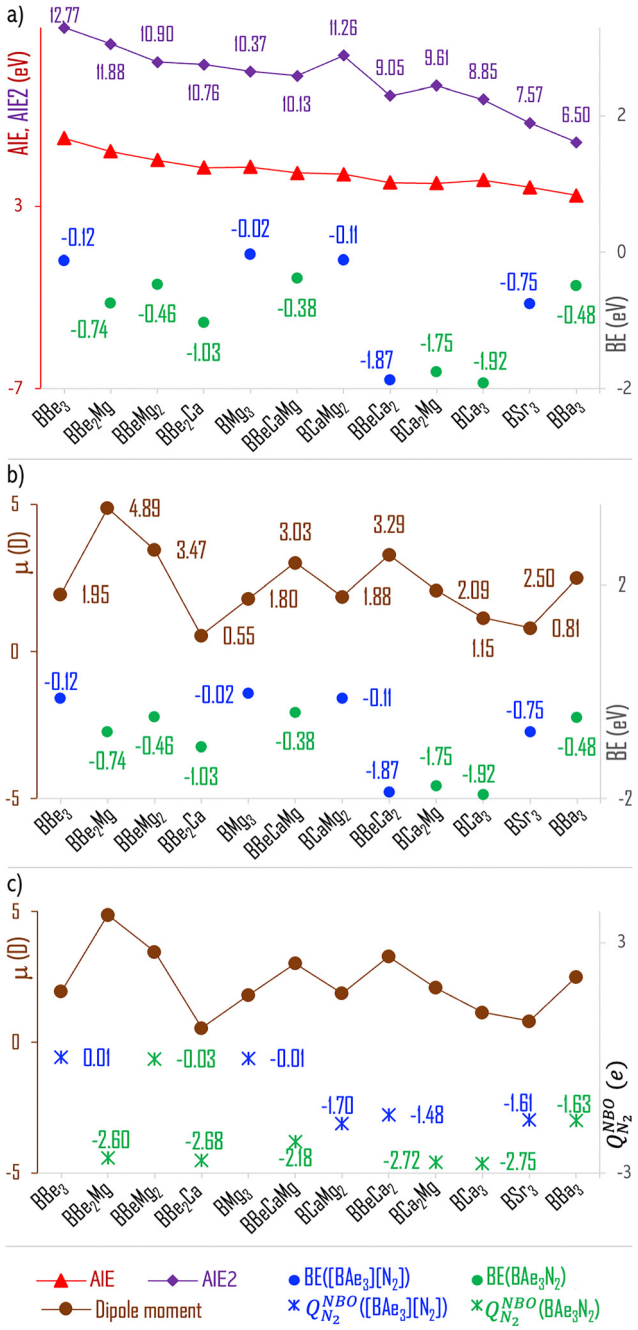

Fig. 14 The first adiabatic ionization energy (AIE, in red), the second adiabatic ionization energy (AIE2, in purple), and dipole moment (μ, in Debye) of BAe_3 clusters. (a) and (b) Binding energy (BE, in eV) of $[BAe_3][N_2]$ (blue circles) and BAe_3N_2 (green circles) species. (c) Charge on N_2 by NBO analysis ($Q_{N_2}^{NBO}$, in e) of $[BAe_3][N_2]$ (blue stars) and BAe_3N_2 (green stars) species. The BAe_3/N_2 systems have been sorted by ascending molecular mass of the BAe_3 subunits.

can activate N_2 through electron donation, leading to bond scission.[65] However, they often require high temperatures or pressures for activation. Electrochemical systems activate N_2 by transferring electrons at electrode surfaces. Yet, they may face efficiency challenges, including sluggish kinetics and high energy barriers. The BAe_3 superalkalis, such as BSr_3, offer a distinct advantage by facilitating N_2 activation under milder conditions, owing to their unique electronic structures and low ionization energies, which promote effective charge transfer without necessitating extreme conditions.

The BAe_3 clusters possess excellent reducibility and can serve as catalysts. Good catalysts adsorb the reactants strongly enough for them to react but should not bind products permanently. Therefore, we consider the above results on the BAe_3/CO_2 and BAe_3/N_2 formation and stability as the first step for the further CO_2 and N_2 transformation into valuable chemicals (such as formic acid, formaldehyde, methanol, or ammonia, respectively). Based on *ab initio* computations, we demonstrated that the reducing ability and reactivity of the BAe_3 clusters can be tuned upon even single atom substitution within the cluster. The ionization energy of the BAe_3 clusters can be precisely controlled by properly chosen alkaline earth metal substituents and predicted from the QSPR model. The suitable electropositive metals with which the central boron atom is decorated can regulate the electronic properties of molecular clusters forming the superalkali. These findings prove that superalkali's properties can be modulated by substituting a single atom within it.

3.13. Catalytic potential – future research

The designed BAe_3 clusters, composed of only four atoms, may have reduced capacity to stabilize certain intermediates compared to larger catalysts. However, their unique electronic properties can be advantageous in specific catalytic applications. Recent studies have demonstrated that small metal clusters, such as those composed of platinum, can efficiently catalyze multi-step reactions.[66] For instance, a study involving fully exposed platinum clusters consisting of an average of four platinum atoms supported on nanodiamond@graphene exhibited excellent catalytic performance, highlighting the efficiency of small clusters in facilitating complex catalytic processes. Therefore, while the small size of BAe_3 clusters may influence their ability to stabilize certain intermediates, their distinctive properties could make them suitable for specific catalytic applications. Further computational and experimental investigations are warranted to fully understand their catalytic potential and to explore their effectiveness in various catalytic processes.

Superalkali clusters can interact with CO_2 and N_2 molecules by donating electrons, which is crucial in electrochemical CO_2 and N_2 reduction. The small size of molecular clusters creates a high density of active sites, which can weaken the C=O and N≡N bonds, making it easier for subsequent steps to occur. Our results are the first step for the BAe_3 clusters' catalytic potential assessment. The next step is to investigate their immobilization on the support. Recently, Huang *et al.*[67] described the catalytic activity of Au_{25} superatoms immobilized on cerium oxide (CeO_2) nanorods for styrene activation. They demonstrated that superatomic clusters immobilized on the CeO_2 nanorods maintain the structural and electronic properties of isolated superatoms. Charge transfer from superatoms to CeO_2 affects the charge distribution of the superatom, which may impact the activation of the oxidant on the superatom and bring about different catalytic selectivities. Future studies on

the catalytic potential of BAe_3 superatoms will at least include superalkali's immobilization on an oxide support (such as CeO_2 and MgO). Investigation of the structural and electronic stability of BAe_3 clusters supported on the surface of oxides will allow us to infer the catalytic mechanism and selectivity towards CO_2 and N_2. These future studies will be crucial in understanding the catalytic mechanism of carbon dioxide and nitrogen reduction, as well as correlating the structural information with catalytic features.

4. Summary

Based on a hybrid QM-QSPR approach, non-mixed and mixed alkaline earth metal systems were proposed here to demonstrate the ability to regulate the electronic properties of a molecular cluster in rationally designing the highly electropositive species, the superalkali. Different from the conventional formulation-assisted methodology, the QSPR strategy predicts the reducing ability of the superalkali, where a suitable alkaline earth metal increases the ionization energy of the resulting BAe_3 cluster *via* the B–Ae and Ae–Ae electrostatic effects. It was observed that the increment of the AIE values of the cluster originates from the sum of the first ionization energies of the constituting atoms, and the alkaline earth metal substitution possesses an intriguing power to modulate the electronic properties of the cluster precisely. Apart from the thermodynamic and electronic stability analysis, the reducing ability of the BAe_3 species was further proved in an interaction with the CO_2 and N_2 systems. We demonstrated that the linear carbon dioxide molecule can be effectively reduced to its anionic bent form by utilizing BAe_3 clusters as reducing agents. From the analysis of the binding energy, the charge transfer, and the geometry of BAe_3/N_2 systems, it follows that the resulting structures can be considered as either the $[BAe_3][N_2]$ complexes or the BAe_3N_2 compounds. We demonstrated that the ionization energy and the dipole moment of the BAe_3 clusters determine the stability and geometry of the resulting BAe_3/N_2 species. The lower ionization energy and larger dipole moment promote the reactivity of the BAe_3 cluster and form stable, strongly bound compounds. Our results emphasize how the structure and stability of the BAe_3/N_2 systems can be tuned upon single atom substitution. All these findings provide new insights into superalkali design, and we hope the QM-QSPR approach highlighted here can stimulate more efforts from both theorists and experimentalists in designing and synthesizing more superalkalis, which can serve as reducing agents in chemical processes.

Author contributions

Natalia Wiszowska: investigation, visualization, and writing – review & editing. Natalia Rogoża: investigation, visualization, and writing – review & editing. Celina Sikorska: conceptualization, supervision, writing – original draft, writing – review & editing, and funding acquisition.

Conflicts of interest

The author declares no conflict of interest.

Data availability

The data supporting this article have been included as part of the supplementary information (SI). Supplementary information: molecular coordinates, lower energy isomers, theory level comparison, thermodynamic stability analysis, mathematical model equations, and QSPR modeling details. See DOI: **https://doi.org/10.1039/d5cp02913a**.

Acknowledgements

This research is part of the project no. 2022/45/P/ST4/01907 co-funded by the National Science Centre and the European Union Framework Programe for Research and Innovation Horizon 2020 under the Marie Skłodowska-Curie grant agreement no. 945339. For the purpose of open access, the author has applied a CC-BY public copyright license to any Author Accepted Manuscript (AAM) version arising from this submission. Calculations have been carried out in (a) the Wroclaw Centre for Networking and Supercomputing (**https://www.wcss.pl**, grant no. 378), (b) the Centre of Informatics–Tricity Academic Supercomputer and Network (CI TASK) in Gdansk (project no. pt01088), and (c) the New Zealand eScience Infrastructure (NeSI) high-performance computing facilities funded jointly by NeSI's collaborator institutions and through the Ministry of Business, Innovation & Employment's Research Infrastructure program (**https://www.nesi.org.nz**, project no. uoa02699). Celina Sikorska would also like to acknowledge support from the Marsden Fund Council from Government Funding administered by the Royal Society of New Zealand (MFP-21-UOA-069). CS would like to express the deepest gratitude to Prof. Adam Liwo for their outstanding mentorship and support throughout this Polonez Bis project.

References

1 C. Sikorska, Design and Investigation of Superatoms for Redox Applications: First-Principles Studies, *Micromachines*, 2024, **15**, 78.
2 J. Simons, Observations on the Electronic Character of Anions and Cations near Water Liquid/Vapor Interfaces, *J. Phys. Chem. A*, 2024, **128**, 8436–8445.
3 G. L. Gutsev and A. I. Boldyrev, Dvm X-Alpha Calculations on the Electronic-Structure of Super-Alkali Cations, *Chem. Phys. Lett.*, 1982, **92**, 262–266.
4 K. Yokoyama, N. Haketa, M. Hashimoto, K. Furukawa, H. Tanaka and H. Kudo, Production of hyperlithiated Li_2F by a laser ablation of LiF–Li_3N mixture, *Chem. Phys. Lett.*, 2000, **320**, 645–650.
5 M. Gutowski and J. Simons, Anionic states of LiFLi, *J. Chem. Phys.*, 1994, **100**, 1308–1311.

6 S. Zein and J. V. Ortiz, Interpretation of the photoelectron spectra of superalkali species: Li_3O and Li_3O, *J. Chem. Phys.*, 2011, **135**, 164307.
7 M. Gutowski and J. Simons, Anionic and Neutral States of Li3O, *J. Phys. Chem.*, 2002, **98**, 8326–8330.
8 A. Otten and G. Meloni, Stability of lithium substituted silyls superalkali species, *Chem. Phys. Lett.*, 2018, **692**, 214–223.
9 W. M. Sun and D. Wu, Recent Progress on the Design, Characterization, and Application of Superalkalis, *Chemistry*, 2019, **25**, 9568–9579.
10 I. R. Ariyarathna, Electronic structure analysis and DFT benchmarking of Rydberg-type alkali-metal-crown ether, -cryptand, and -adamanzane complexes, *Phys. Chem. Chem. Phys.*, 2024, **26**, 16989–16997.
11 G. N. Reddy and S. Giri, Organic heterocyclic molecules become superalkalis, *Phys. Chem. Chem. Phys.*, 2016, **18**, 24356–24360.
12 I. Anusiewicz, Superalkali Molecules Containing Halogenoids, *J. Theor. Comput. Chem.*, 2012, **10**, 191–208.
13 I. Świerszcz and I. Anusiewicz, Low ionization potentials of Na4OCN superalkali molecules, *Mol. Phys.*, 2011, **109**, 1739–1748.
14 S. Giri, G. N. Reddy and P. Jena, Organo-Zintl Clusters $[P_7R_4]$: A New Class of Superalkalis, *J. Phys. Chem. Lett.*, 2016, **7**, 800–805.
15 Y. Li, D. Wu, Z. R. Li and C. C. Sun, Structural and electronic properties of boron-doped lithium clusters: ab initio and DFT studies, *J. Comput. Chem.*, 2007, **28**, 1677–1684.
16 Y. J. Wang, L. Y. Feng and H. J. Zhai, Sandwich-type Na(6)B(7)(−) and Na(8)B(7)(+) clusters: charge-transfer complexes, four-fold pi/sigma aromaticity, and dynamic fluxionality, *Phys. Chem. Chem. Phys.*, 2019, **21**, 18338–18345.
17 C. Sikorska and N. Gaston, N_4Mg_6M (M = Li, Na, K) superalkalis for CO_2 activation, *J. Chem. Phys.*, 2020, **153**, 144301.
18 D. Yu, D. Wu, J. Y. Liu, Y. Li and W. M. Sun, Unveiling the potential of superalkali cation Li_3^+ for capturing nitrogen, *Phys. Chem. Chem. Phys.*, 2020, **22**, 26536–26543.
19 H. Park and G. Meloni, Activation of Dinitrogen with a Superalkali Species, Li_3F_2, *ChemPhysChem*, 2018, **19**, 256–260.
20 S. Sarkar, T. Debnath and A. K. Das, Superalkalis with Hydrogen as Central Electronegative Atom and their Possible Applications: Ab Initio and DFT Study, *Chemistry*, 2024, **30**, e202304223.
21 C. Sikorska, E. Vincent, A. Schnepf and N. Gaston, Tuning the electronic structure of gold cluster-assembled materials by altering organophosphine ligands, *Phys. Chem. Chem. Phys.*, 2024, **26**, 10673–10687.
22 C. Sikorska and N. Gaston, Molecular crystals vs. superatomic lattice: a case study with superalkali-superhalogen compounds, *Phys. Chem. Chem. Phys.*, 2022, **24**, 8763–8774.
23 Y. F. Wang, T. Qin, J. M. Tang, Y. J. Liu, M. Xie, J. Li, J. Huang and Z. R. Li, Novel inorganic aromatic mixed-valent superalkali electride CaN(3)Ca: an alkaline-earth-based high-sensitivity multi-state nonlinear optical molecular switch, *Phys. Chem. Chem. Phys.*, 2020, **22**, 5985–5994.
24 H. R. Banjade, D. Deepika, S. Giri, S. Sinha, H. Fang and P. Jena, Role of Size and Composition on the Design of Superalkalis, *J. Phys. Chem. A*, 2021, **125**, 5886–5894.
25 S. Giri, S. Behera and P. Jena, Superalkalis and Superhalogens As Building Blocks of Supersalts, *J. Phys. Chem. A*, 2014, **118**, 638–645.
26 E. S. O'Brien, M. T. Trinh, R. L. Kann, J. Chen, G. A. Elbaz, A. Masurkar, T. L. Atallah, M. V. Paley, N. Patel, D. W. Paley, I. Kymissis, A. C. Crowther, A. J. Millis, D. R. Reichman, X. Y. Zhu and X. Roy, Single-crystal-to-single-crystal intercalation of a low-bandgap superatomic crystal, *Nat. Chem.*, 2017, **9**, 1170–1174.
27 X. Roy, C. H. Lee, A. C. Crowther, C. L. Schenck, T. Besara, R. A. Lalancette, T. Siegrist, P. W. Stephens, L. E. Brus, P. Kim, M. L. Steigerwald and C. Nuckolls, Nanoscale atoms in solid-state chemistry, *Science*, 2013, **341**, 157–160.
28 S. Ji, Y. Chen, Q. Fu, Y. Chen, J. Dong, W. Chen, Z. Li, Y. Wang, L. Gu, W. He, C. Chen, Q. Peng, Y. Huang, X. Duan, D. Wang, C. Draxl and Y. Li, Confined Pyrolysis within Metal-Organic Frameworks To Form Uniform Ru(3) Clusters for Efficient Oxidation of Alcohols, *J. Am. Chem. Soc.*, 2017, **139**, 9795–9798.
29 W. Ren, X. Tan, W. Yang, C. Jia, S. Xu, K. Wang, S. C. Smith and C. Zhao, Isolated diatomic Ni-Fe metal–nitrogen sites for synergistic electroreduction of CO2, *Angew. Chem., Int. Ed.*, 2019, **58**, 6972–6976.
30 J. Jiao, R. Lin, S. Liu, W.-C. Cheong, C. Zhang, Z. Chen, Y. Pan, J. Tang, K. Wu and S.-F. Hung, Copper atom-pair catalyst anchored on alloy nanowires for selective and efficient electrochemical reduction of CO2, *Nat. Chem.*, 2019, **11**, 222–228.
31 J. Zheng and R. M. Dickson, Individual water-soluble dendrimer-encapsulated silver nanodot fluorescence, *J. Am. Chem. Soc.*, 2002, **124**, 13982–13983.
32 L. Zhang, R. Si, H. Liu, N. Chen, Q. Wang, K. Adair, Z. Wang, J. Chen, Z. Song and J. Li, Atomic layer deposited Pt-Ru dual-metal dimers and identifying their active sites for hydrogen evolution reaction, *Nat. Commun.*, 2019, **10**, 4936.
33 H. Wang, J.-X. Liu, L. F. Allard, S. Lee, J. Liu, H. Li, J. Wang, J. Wang, S. H. Oh, W. Li, M. Flytzani-Stephanopoulos, M. Shen, B. R. Goldsmith and M. Yang, Surpassing the single-atom catalytic activity limit through paired Pt-O-Pt ensemble built from isolated Pt1 atoms, *Nat. Commun.*, 2019, **10**, 3808.
34 J. Wang, Z. Huang, W. Liu, C. Chang, H. Tang, Z. Li, W. Chen, C. Jia, T. Yao, S. Wei, Y. Wu and Y. Li, Design of N-Coordinated Dual-Metal Sites: A Stable and Active Pt-Free Catalyst for Acidic Oxygen Reduction Reaction, *J. Am. Chem. Soc.*, 2017, **139**, 17281–17284.
35 X. L. Zhang, Y. L. Ye, L. Zhang, X. H. Li, D. Yu, J. H. Chen and W. M. Sun, Designing an alkali-metal-like superatom Ca(3)B for ambient nitrogen reduction to ammonia, *Phys. Chem. Chem. Phys.*, 2021, **23**, 18908–18915.
36 M. S. Hill, D. J. Liptrot and C. Weetman, Alkaline earths as main group reagents in molecular catalysis, *Chem. Soc. Rev.*, 2016, **45**, 972–988.
37 J. Y. Liu, Y. J. Xi, Y. Li, S. Y. Li, D. Wu and Z. R. Li, Does Alkaline-Earth-Metal-Based Superalkali Exist?, *J. Phys. Chem. A*, 2016, **120**, 10281–10288.

38 R. Krishnan, J. S. Binkley, R. Seeger and J. A. Pople, Self-consistent molecular orbital methods. XX. A basis set for correlated wave functions, *J. Chem. Phys.*, 1980, **72**, 650–654.
39 F. Weigend, Accurate Coulomb-fitting basis sets for H to Rn, *Phys. Chem. Chem. Phys.*, 2006, **8**, 1057–1065.
40 F. Weigend and R. Ahlrichs, Balanced basis sets of split valence, triple zeta valence and quadruple zeta valence quality for H to Rn: Design and assessment of accuracy, *Phys. Chem. Chem. Phys.*, 2005, **7**, 3297–3305.
41 M. J. Frisch, G. W. Trucks, H. B. Schlegel, G. E. Scuseria, M. A. Robb, J. R. Cheeseman, G. Scalmani, V. Barone, G. A. Petersson, H. Nakatsuji, X. Li, M. Caricato, A. V. Marenich, J. Bloino, B. G. Janesko, R. Gomperts, B. Mennucci, H. P. Hratchian, J. V. Ortiz, A. F. Izmaylov, J. L. Sonnenberg, D. Williams-Young, F. Ding, F. Lipparini, F. Egidi, J. Goings, B. Peng, A. Petrone, T. Henderson, D. Ranasinghe, V. G. Zakrzewski, J. Gao, N. Rega, G. Zheng, W. Liang, M. Hada, M. Ehara, K. Toyota, R. Fukuda, J. Hasegawa, M. Ishida, T. Nakajima, Y. Honda, O. Kitao, H. Nakai, T. Vreven, K. Throssell, J. A. Montgomery Jr., J. E. Peralta, F. Ogliaro, M. J. Bearpark, J. J. Heyd, E. N. Brothers, K. N. Kudin, V. N. Staroverov, T. A. Keith, R. Kobayashi, J. Normand, K. Raghavachari, A. P. Rendell, J. C. Burant, S. S. Iyengar, J. Tomasi, M. Cossi, J. M. Millam, M. Klene, C. Adamo, R. Cammi, J. W. Ochterski, R. L. Martin, K. Morokuma, O. Farkas, J. B. Foresman and D. J. Fox, *Gaussian 16 Rev. C.01.*, Wallingford, CT, 2016, Gaussian 16 Rev. B.01.
42 T. Lu and F. Chen, Multiwfn: a multifunctional wavefunction analyzer, *J. Comput. Chem.*, 2012, **33**, 580–592.
43 T. Lu, A comprehensive electron wavefunction analysis toolbox for chemists, Multiwfn, *J. Chem. Phys.*, 2024, **161**, 082503.
44 Chemcraft – graphical software for visualization of quantum chemistry computations. Version 1.8, build 682. **https://www.chemcraftprog.com**.
45 M. Haranczyk and M. Gutowski, Visualization of Molecular Orbitals and the Related Electron Densities, *J. Chem. Theory Comput.*, 2008, **4**, 689–693.
46 OECD 2007 Guidance Document on the Validation of (Quantitative) Structure–Activity Relationships [(Q)SAR] Models. OECD Environment Health and Safety Publications Series on Testing and Assessment No. 69 ENV/JM/MONO(2007)2 Paris: Organisation for Economic Co-operation and Development.
47 C. Sikorska, Toward predicting vertical detachment energies for superhalogen anions exclusively from 2-D structures, *Chem. Phys. Lett.*, 2015, **625**, 157–163.
48 A. C. Atkinson, *Plots, transformations, and regression an introduction to graphical methods of diagnostic regression analysis,* Oxford University, Oxford, 1985.
49 C. Sikorska, D. Ignatowska, S. Freza and P. Skurski, The Performance of Selected Ab Initio Methods in Estimating Electron Binding Energies of Superhalogen Anions, *J. Theor. Comput. Chem.*, 2012, **10**, 93–109.
50 J. Simons and M. Gutowski, Double-Rydberg molecular anions, *Chem. Rev.*, 2002, **91**, 669–677.
51 K. Bowen, J. Eaton, R. Naaman and Z. Vager, in *The structure of small molecules and ions*. ed. R. Naarnna and Z. Vagar, 1988.
52 J. V. Ortiz, Vertical and adiabatic ionization energies of NH-4 isomers via electron propagator theory and many body perturbation theory calculations with large basis sets, *J. Chem. Phys.*, 1987, **87**, 3557–3562.
53 H. Hopper, M. Lococo, O. Dolgounitcheva, V. G. Zakrzewski and J. V. Ortiz, Double-Rydberg Anions: Predictions on NH3AHn- and OH2AHn- Structures, *J. Am. Chem. Soc.*, 2000, **122**, 12813–12818.
54 S. Giri, G. N. Reddy and P. Jena, Organo-Zintl Clusters $[P_7R_4]$: A New Class of Superalkalis, *J. Phys. Chem. Lett.*, 2016, **7**, 800–805.
55 A. Tlahuice-Flores, D. M. Black, S. B. Bach, M. Jose-Yacaman and R. L. Whetten, Structure & bonding of the gold-subhalide cluster I-Au144Cl60[z], *Phys. Chem. Chem. Phys.*, 2013, **15**, 19191–19195.
56 E. Roduner, C. Jensen, J. van Slageren, R. A. Rakoczy, O. Larlus and M. Hunger, Anomalous diamagnetic susceptibility in 13-atom platinum nanocluster superatoms, *Angew. Chem., Int. Ed.*, 2014, **53**, 4318–4321.
57 S. F. R. Taylor, S. A. Brittle, P. Desai, J. Jacquemin, C. Hardacre and W. A. Zimmerman, Factors affecting bubble size in ionic liquids, *Phys. Chem. Chem. Phys.*, 2017, **19**, 14306–14318.
58 Y. Zhao, Y. Huang, X. Zhang and S. Zhang, A quantitative prediction of the viscosity of ionic liquids using S(sigma-profile) molecular descriptors, *Phys. Chem. Chem. Phys.*, 2015, **17**, 3761–3767.
59 A. C. Atkinson, *Plots, transformations, and regression an introduction to graphical methods of diagnostic regression analysis*, 1985.
60 H. Park and G. Meloni, Reduction of carbon dioxide with a superalkali, *Dalton Trans.*, 2017, **46**, 11942–11949.
61 T. Zhao, Q. Wang and P. Jena, Rational design of superalkalis and their role in CO_2 activation, *Nanoscale*, 2017, **9**, 4891–4897.
62 A. K. Srivastava, Single- and double-electron reductions of CO2 by using superalkalis: An ab initio study, *Int. J. Quantum Chem.*, 2018, **118**, e25598.
63 H. Song and H. Guo, Theoretical Insights into the Dynamics of Gas-Phase Bimolecular Reactions with Submerged Barriers, *ACS Phys. Chem. Au*, 2023, **3**, 406–418.
64 H. Srivastava, A. Kumar Srivastava and N. Misra, Interaction of N(2), O(2) and H(2) Molecules with Superalkalis, *ChemistryOpen*, 2024, **13**, e202300253.
65 A. Januszewska-Kubsik, S. Podsiadło, W. Pudełko and M. Siekierski, Metal nitrides as electrocatalysts in green ammonia synthesis, *Appl. Phys. A:Mater. Sci. Process.*, 2024, **130**, 771.
66 Y. Si, Y. Jiao, M. Wang, S. Xiang, J. Diao, X. Chen, J. Chen, Y. Wang, D. Xiao, X. Wen, N. Wang, D. Ma and H. Liu, Fully exposed Pt clusters for efficient catalysis of multi-step hydrogenation reactions, *Nat. Commun.*, 2024, **15**, 4887.
67 P. Huang, G. X. Chen, Z. Jiang, R. C. Jin, Y. Zhu and Y. H. Sun, Atomically precise Au_{25} superatoms immobilized on CeO_2 nanorods for styrene oxidation, *Nanoscale*, 2013, **5**, 3668–3672.